Marine Environmental Research 196 (2024) 106371

Contents lists available at ScienceDirect

Marine Environmental Research

journal homepage: www.elsevier.com/locate/marenvrev

Phytoplankton assemblage responses to nitrogen following COVID-19 stay–in–place orders in western Long Island Sound (New York/Connecticut)

Maximillian Brown [a,b], Mariapaola Ambrosone [b], Kyle J. Turner [c], Georgie E. Humphries [a,b], Maria Tzortziou [c], Sílvia Anglès [b,1], Caterina Panzeca [d], Dianne I. Greenfield [a,b,*]

[a] School of Earth and Environmental Sciences, Queens College, City University of New York, Flushing, NY, 11367, USA
[b] Advanced Science Research Center at the Graduate Center, City University of New York, New York, NY, 10031, USA
[c] Earth and Atmospheric Science, Center for Discovery and Innovation, The City College of New York, City University of New York, New York, NY, 10031, USA
[d] State University of New York Maritime College, Bronx, NY, 10465, USA

ARTICLE INFO

Keywords:
Bioassay
Coronavirus
Diatoms
Ecosystem management
Nitrogen
Algal blooms
Estuary
Urbanization
Wastewater

ABSTRACT

This study evaluated water quality, nitrogen (N), and phytoplankton assemblage linkages along the western Long Island Sound (USA) shoreline (Nov. 2020–Dec. 2021) following COVID-19 stay-in-place (SIP) orders through monthly surveys and N-addition bioassays. Ammonia-N (AmN; NH_3+NH_4^+) negatively correlated with total chlorophyll-*a* (chl-*a*) at all sites; this was significant at Alley Creek, adjacent to urban wastewater inputs, and at Calf Pasture, by the Norwalk River (Spearman rank correlation, $p < 0.01$ and 0.02). Diatoms were abundant throughout the study, though dinoflagellates (*Heterocapsa*, *Prorocentrum*), euglenoids/cryptophytes, and both nano- and picoplankton biomass increased during summer. In field and experimental assessments, high nitrite + nitrate (N + N) and low AmN increased diatom abundances while AmN was positively linked to cryptophyte concentrations. Likely N + N decreases with presumably minimal changes in AmN and organic N during COVID-19 SIP resulted in phytoplankton assemblage shifts (decreased diatoms, increased euglenoids/cryptophytes), highlighting the ecological impacts of N-form delivered by wastewater to urban estuaries.

1. Introduction

Long Island Sound (LIS), USA, is a large (average 160 km length x 20 km width x 21 m depth) nitrogen (N) enriched urban estuary (Gay et al., 2004; Vaudrey 2017; Vlahos et al., 2020; Long Island Sound Study 2021). LIS exchanges tides diurnally with both the East River in New York City (NYC, western boundary) and the Atlantic Ocean (eastern boundary) while receiving 80% of freshwater inputs from rivers, primarily the Thames, Housatonic, and Connecticut (CT) rivers (Gay et al., 2004; O'Donnell et al., 2014). Riverine inputs (including the East River) supply ~23.5×10^6 kg N y^{-1} of total N (TN) to LIS, with atmospheric deposition contributing ~2.8×10^6 kg N y^{-1} (Vlahos et al., 2020). This N load contributes to algal bloom formation in LIS and nearby embayments, as well as LIS summer hypoxia from microbial respiration of organic matter (e.g., sewage, phytoplankton) alongside environmental forcings (Hattenrath et al., 2010; Hattenrath-Lehmann et al., 2015; Whitney and Vlahos 2021).

Overall N levels decline along an urban-suburban transition (NYC-CT) from the heavily developed Western Narrows to eastern LIS (Vaudrey et al., 2016). In tandem, the sources of N inputs become a more diverse mixture of sewage, atmospheric, and fertilizer origins (Vaudrey et al., 2016; Vlahos et al., 2020). For example, 97% of the East River N load to the Western Narrows comes from NYC sewage, namely wastewater (WW) treatment effluent and combined sewage overflows (CSOs) (Vaudrey et al., 2016). CT N inputs include sewage and septic (77%), atmospheric deposition (12%), and fertilizers (10%) to Norwalk Harbor compared to septic systems (41%), fertilizers (30%), and atmospheric deposition (25%) moving east to the Saugatuck River (SR) estuary (Vaudrey et al., 2016; Tetra Tech, 2018). This is partially due to differing land uses; the Western Narrows' watershed is 86% developed whereas the SR watershed is 20% developed, reflecting lower human population density along the CT coast (NYC 29,303 persons mi^{-2} [11,311 persons km^{-2}] versus Westport CT 1360 persons mi^{-2} [525 persons km^{-2}]) (Tetra Tech, 2018; United States Census Bureau, 2020; 2022).

The concentration of WW effluent in the East River and Western Narrows influences summer bottom water hypoxia in western LIS

* Corresponding author. School of Earth and Environmental Sciences, Queens College, City University of New York, Flushing, NY, 11367, USA.
E-mail address: dgreenfield@gc.cuny.edu (D.I. Greenfield).
[1] Current address: California Department of Water Resources, 3500 Industrial Blvd, West Sacramento, CA 95691.

https://doi.org/10.1016/j.marenvres.2024.106371
Received 1 September 2023; Received in revised form 5 December 2023; Accepted 17 January 2024
Available online 22 January 2024

(WLIS), where the highest concentrations of chlorophyll *a* (chl-*a*) in the estuary are also found (Li et al., 2018; Perreira, 2021; Whitney and Vlahos 2021; Roldan-Ayala et al., 2023). To manage LIS hypoxia, a total maximum daily load for point-source TN inputs was mandated by the Environmental Protection Agency (EPA) in 2001 (EPA National Estuary Program, 2022). Subsequent upgrades to WW treatment (WWT) plants resulted in a 60% TN decrease by 2016 relative to the 1994 baseline and a 50% reduction in total hypoxic area, though seasonal WLIS hypoxia recurs (Vaudrey 2017; Vlahos et al., 2020; CT Department of Energy and Environmental Protection (CT-DEEP, 2021; Whitney and Vlahos 2021). Despite treatment methods, WW effluent contains significant amounts of remaining ammonia and ammonium (NH_3+NH_4^+, hereafter AmN), and dissolved organic N (DON), due to difficulty in removal (Trygar 2009; Mallick et al., 2022; NYC-DEP, 2022b). WWT upgrades resulted in lower median dissolved inorganic N (DIN) concentrations, and decreased DIN: DON within surface and bottom WLIS waters (2002–2021) that are associated with reductions in nitrate and nitrite (NO_3^- + NO_2^-, hereafter N + N) (Suter et al., 2014; Yao et al., 2019; CT-DEEP 2021; Whitney and Vlahos 2021).

Available chemical form and concentrations of N differentially influence phytoplankton growth and community structure in eutrophic and developed waterways (Cira et al., 2016; Reed et al., 2016; Sitta et al., 2018). Since WWT upgrades, there have been no consistent long-term temporal trends in total chl-*a* when considering the whole LIS; however, DIN:DON decreases were associated with transitions in the dominant phytoplankton taxa (Suter et al., 2014; CT-DEEP 2021; Whitney and Vlahos 2021). High performance liquid chromatography (HPLC) pigment analysis of samples from stations routinely monitored by CT-DEEP (2002–2014) in the WLIS mainstem (offshore) revealed the proportion of diatoms decreased relative to mixotrophs, including dinoflagellates (such as *Prorocentrum* species), cryptophytes, and euglenoids (Suter et al., 2014).

Compared to the number and frequency of WLIS offshore surveys (e.g., by CT-DEEP), there have been few studies of nearshore phytoplankton communities. Characterizing these processes is important because nearshore phytoplankton communities display variability in their physiological responses to environmental cues (light availability, salinity, and seasonality) and heterogeneous episodes of nutrient loading (Romero et al., 2014; Lemley et al., 2019). Prior work noted nearshore WLIS phytoplankton assemblages are variously composed of diatoms, euglenoids, cryptophytes, and dinoflagellates, but few studies have interrogated how N influences nearshore species composition in this region (Greenfield et al., 2005; Gobler et al., 2006; Li et al., 2018; Van Gulick 2020). Mechanisms driving site-specific assemblage differences related to N-form/concentration are consequently understudied. Since N form and composition of WW effluent and raw sewage has been linked to a smaller proportion of diatoms relative to other phytoplankton, as well as conditions favoring harmful algal bloom (HAB) formation in LIS and other estuarine and freshwater systems (McCarthy et al., 2009; Gobler et al., 2012; Hattenrath et al., 2010; Schweitzer 2019; Glibert et al., 2022), connecting N-form and levels at the land-water interface with phytoplankton assemblages can inform LIS water quality management.

Spatial transitions in terrestrial N inputs along the NYC-CT urban-suburban gradient likely influence nearshore phytoplankton taxonomic composition. However, these connections can be difficult to identify in the temporal context of declining DIN:DON, seasonality, and climate change (Vaudrey et al., 2016; Whitney and Vlahos 2021). Regional perturbations in anthropogenic activity – either through acceleration or deceleration - offer opportunities for mechanistic insight into how human activity impacts coastal ecosystem responses.

Coined the "anthropause" (Rutz et al., 2020), the period spanning COVID-19 stay in place (SIP) orders and subsequent phased re-entry provides a unique window into how changes in human activity affects ecosystem function. To date, few published works have examined relationships between estuarine water quality, nutrients, chl-*a*, and phytoplankton assemblages during COVID-19 SIP, many of which incorporated satellite data. As examples, remote sensing observations off the coast of the Yellow Sea, Venice, and the Arabian coast of India documented 30%, 100% and 30% decreases in chl-*a* (Apr. and May 2020 compared to baselines in 2015–2019, 2017–19, and 2018, respectively) (Mishra et al., 2020; Braga et al., 2022; Yoon et al., 2022). During 2020, in Blanes Bay on the Mediterranean coast, water samples revealed small decreases in total chl-*a* and N + N (Sala et al., 2022), whereas Kuwait Bay satellite observations of chl-*a* increases were associated with DIN increases and a dinoflagellate bloom (Polikarpov et al., 2021). Lower riverine AmN concentrations in China (Apr. and May 2020 versus 2018–2019) were attributed to sewage reductions (Liu et al., 2022).

During this study (Nov. 2020–Dec. 2021), a NY State disaster emergency was in effect (07 Mar. 2020–24 June 2021) in response to the COVID-19 pandemic (New York State Governor, 2021). Changes in human mobility altered spatial patterns of N discharge to LIS, as N discharged into the Eastern Narrows decreased by 10% during the shutdown (Sherman et al., 2023b) likely due to less WW derived N. Concomitant reductions in atmospheric NO_2 levels (21–36% decreases in NY/CT from 2018, Tzortziou et al., 2022) during the spring-summer 2020 shutdown were attributed to fewer commuters: the number of people working remotely in the NYC metropolitan region increased 500% compared to 2017–2019 (Sherman et al., 2023b). A second decline in atmospheric NO_x was measured late 2020-early 2021, coincident with a resurgence in SIP measures during the second pandemic wave in the NY metropolitan region (Tzortziou et al., 2022). Given these short-term air quality improvements related to N, it is conceivable that as remote work increased, patterns of WW effluent and other sources of terrestrially derived N inputs from NYC/CT to WLIS shifted, impacting phytoplankton community composition and biomass (chl-*a*); in WLIS, there was a 40% decrease in remotely-sensed chl-*a* during Apr. 2020 relative to 2017–2019 (Sherman et al., 2023b), though precise causal mechanisms remain unclear.

The goal of this study was to characterize nearshore phytoplankton assemblages in WLIS, specifically along the NYC-CT commuting corridor, during and following COVID-19 SIP as they relate to N-form/concentration. This was achieved through the following objectives: 1) assess the relationships between phytoplankton assemblages and N-form/concentration at nearshore sites during and following COVID-19 SIP; 2) experimentally quantify phytoplankton assemblage responses to N-form via *in situ* nutrient addition bioassays at western and eastern ends of the study area by mimicking pre-COVID-19 N conditions. Study results help disentangle the relationships between N-form and proximity to point source N-inputs on phytoplankton assemblages while informing water quality management strategies.

2. Materials and methods

2.1. Field surveys

Water sampling was conducted monthly ~2–3 h before low tide from 11 Nov. 2020–03 Dec. 2021 at WLIS shore sites spanning an urban-suburban gradient along the NYC-CT commuting corridor.

2.1.1. Sampling sites

Shore sites, Alley Creek (AC), City Island (CI), Rye Playland (RP), Calf Pasture (CP), and the Saugatuck River (SR) (Fig. 1), ranged 0.3 (AC)-3.0 m (RP) depth at low tide (NOAA 2023) and were selected to capture N entering the estuary from rivers, wastewater outfalls, and terrestrial sources. AC (40.7633, −73.7518) is adjacent to three CSOs and the Alley Pond Golf Center near the East River-WLIS confluence. A pollution control plan for AC was approved to create a CSO disinfection system with United States Geological Survey measurements of suspended solids, pharmaceuticals, and fecal bacterial markers (Aug. 2020–June 2021) (New York State Department of Environmental Conservation, 2017; Fisher et al., 2022). CI (40.8540, −73.7871) is located

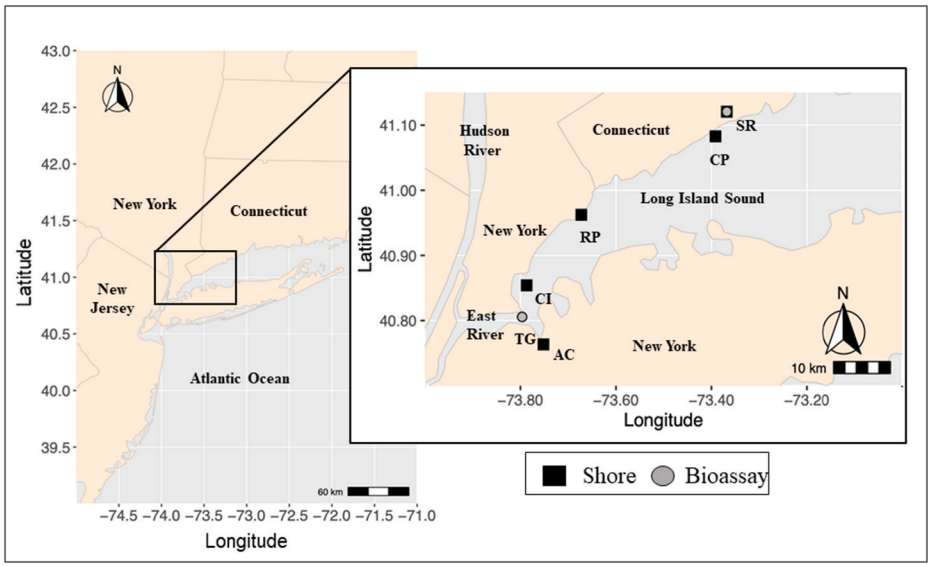

Fig. 1. Map of study region with insert denoting shore sampling and bioassay sites. Shore sites (squares) are Alley Creek (AC), City Island (CI), Rye Playland (RP), Calf Pasture (CP), and Saugatuck River (SR). Bioassay sites (circles) Throggs Neck (TG) and SR are also shown. Note that SR is both a shore sampling and bioassay site.

within the Eastern Narrows on an eastward facing dock ~1 km north of a sewage outfall and near NYC-DEP monitoring station E8 (from which available N + N, AmN, and total Kjeldahl N (TKN) data (Jan. 2010–June 2019) were leveraged to inform pre-COVID conditions) (NYDEP 2022a; New York State, 2022; data.nyc.gov). RP (40.9624, −73.6726) is on a southeastern facing dock adjacent to the Edith G. Read Natural Park and Wildlife Sanctuary that spatially connects western (urban) and eastern (suburban) locations (data.nyc.gov) and unique among sites because it is neither adjacent to riverine inputs nor CSOs; as such, water was presumably of relatively greater marine origin. CP (41.0828, −73.3815) is on a southern facing dock adjacent to the Norwalk River and the Norwalk shellfish biotoxin monitoring station (CT Department of Agriculture, Bureau of Aquaculture, Town Code 103), with the Northport Water Pollution Control Facility ~1 km upstream (Tetra Tech, 2018; Van Gulick 2020). SR (41.1207, −73.3678) is a floating dock ~1 km north of the Saugatuck River-LIS confluence and the Longshore Golf Course, opposite the Westport Town Sewer Treatment Facility (Tetra Tech, 2018) and was surveyed (N + N, AmN, and TN) by the citizen science group Norwalk Harbor Watch in 2020 (Norwalk Harbor Watch, unpublished data).

2.1.2. *Sample collection and physical water quality*

From each shore site, water samples (0.3–0.5 m depth) were collected using a 2.2 L Niskin bottle. Samples were then dispensed into previously acid washed (10% hydrochloric acid for ≥4 h, rinsed three times with reverse osmosis water) 1 L opaque high-density polyethylene Nalgene® bottles (n = 3), placed in a cooler on cold packs, and transported to the laboratory within 2 h of collection for processing of nutrients, chl-*a*, and phytoplankton community composition (Section 2.3).

At all sites, water quality (temperature (T), salinity (S), dissolved oxygen (DO), pH, and turbidity) was measured using a YSI EXO2 sonde. Daily precipitation data were obtained from National Oceanic and Atmospheric Administration (NOAA) National Weather Service (NWS) stations at (west to east) LaGuardia Airport, Larchmont NY (Larchmont 1.1 NE), and Norwalk CT (Norwalk 1.4 ENE) (NWS, 2022), converted from inches to mm, then summed as cumulative precipitation 7 days before each sampling.

2.2. *In situ bioassays*

To determine whether N-form and levels following COVID-19 SIP affected phytoplankton biomass and species composition, nutrient addition bioassays were conducted *in situ* (native light and temperature conditions) by mimicking pre-COVID-19 N concentrations. These experiments were located at the geographic ends of the survey range to assess spatial influences of N on phytoplankton assemblages. Incubations took place in 2021 on floating docks at the State University of NY Maritime College Olivet Pier at Throggs Neck (TG, 40.8055, −73.7965, 7–10 Sept.) and SR (14–17 Sept.) (Fig. 1). TG is ~0.5 km east of a CSO and adjacent to NYC-DEP sampling station E8. Measurements from Norwalk Harbor Watch in Sept. 2020 (personal communication) were used to determine SR baselines (Table S1). Based on these assessments, N was added to a final concentration of +20 μM per atom N (calculated for final volume) as NH_4+ (as ammonium chloride, NH_4Cl, Sigma-Aldrich®, product#A9434), NO_3^- (as potassium nitrate, KNO_3, Fisher Chemical™, product #P2631000) or urea ($CO(NH_2)_2$, Sigma Aldrich®, product #U5378) to test reduced, oxidized, and organic N-forms, respectively. PO_4^{3-} (dissolved inorganic phosphorus, DIP) (as potassium phosphate monobasic, KH_2PO_4, Sigma Aldrich®, product #57618) was added at 'Redfield' elemental ratios (16:1 N:P per atom; Redfield 1958) to avoid co-limitation of phosphorus for phytoplankton (Reed et al., 2016; Sitta et al., 2018). Each bioassay had six treatments (three replicates per treatment): control with no additions (C), phosphate (P), nitrate + phosphate (NP), ammonium + phosphate (AP), urea + phosphate (UP), and all N-forms at equal atom levels + phosphate (ALL). Surface water (0.2 m depth) collection and N-additions occurred within 2 h after high tide.

Surface physical water quality (T, S, DO, pH, and turbidity) was recorded at the experimental start (t (0)) and each timepoint using a YSI ProSolo sonde and a handheld Mettler Toledo Seven 2Go pH meter. The light extinction coefficient (k) was calculated from the Secchi depth (Brown 1984). To determine t (0) nutrient and phytoplankton conditions, surface water was collected and dispensed to previously acid-washed (as above) 1 L Nalgene® bottles (n = 3). For all replicates, surface water was collected using a 5 L plastic beaker then dispensed into 2 L Thermo Scientific Nalgene® transparent polycarbonate bottles (manufacturer #20152000) pre-rinsed 3× with surface water onsite. After nutrient addition, bottles were closed and secured to the dock in a large mesh bag (hand stitched from black polyethylene tarp, Harbor Freight #60577) to achieve 30–40% surface irradiance and avoid phytoplankton photoquenching (Reed et al., 2015; Sitta et al., 2018), then incubated at the water surface for 72 h. This incubation time frame

effectively assessed phytoplankton community composition changes without risking nutrient depletion (Pinckney et al., 2020). Each bottle was sub-sampled at t (24) (24 h, to capture short-term N-uptake and allow gas exchange) and removed at t (72) (final, to capture assemblage shifts). During sub-sampling, each bottle was gently inverted several times to mix the incubation water, then 200 mL was decanted into a graduated cylinder and allocated into 500 mL opaque high-density polyethylene Nalgene® bottles. Treatment bottles were randomly returned to the mesh bag and placed *in situ* for the remaining incubation. All water samples were kept cool and in the dark, and immediately transported to the laboratory where replicates were processed for subsequent nutrient, chl-*a*, and phytoplankton (species abundances) analysis per timepoint (Section 2.3). DON was calculated as TDN - DIN, and dissolved organic phosphorus (DOP) was calculated as TDP - DIP. Phytoplankton instantaneous growth rates were calculated per replicate using the following equation (Reed et al., 2016):

$$\frac{lnX_{t2} - lnX_{t1}}{\Delta t}$$

Where X is the concentration of phytoplankton cells or chl-*a* at timepoint t (days) for a particular cell size fraction and Δt is elapsed time. To assess changes in nutrient concentrations relative to algal biomass, phytoplankton uptake rates (V_{N+N}, V_{AmN}, V_{DIP}, and V_{Si}) were calculated per replicate using the following equation (Conway et al., 1976):

$$\frac{S_{t2} - S_{t1}}{(\Delta t)(Y)}$$

Where S is the nutrient concentration at timepoint t (days), and Y is biomass at t_2.

2.3. Analytical methods

2.3.1. Nutrients

Upon return to the laboratory, aliquots of water (~17 mL) from each replicate were passed through previously acid-washed 60 mL syringes affixed with 0.7 μm, 25 mm diameter glass microfiber filters (GF/Fs) (Whatman™ Cytiva, product #1825–025) into acid washed 20 mL glass scintillation vials for analysis of AmN, N + N, TDN, DIP, and TDP. Dissolved Si was similarly processed, but into plastic vials. All samples were frozen (−20 °C) until colorimetric analysis using a Lachat Quickchem® 8500 autoanalyzer (Zimmerman and Keefe 1991; Grasshoff et al., 1999; Hales et al., 2004).

2.3.2. Chl-*a*

Unfiltered water aliquots (40 mL) were used to determine total chl-*a* concentrations, while samples filtered through <20 μm and <5 μm Nitex® nylon mesh screens were used to determine relative contributions of micro-, nano-, and picophytoplankton to overall chl-*a* (Greenfield et al., 2005; Lonsdale et al., 2006). All samples were passed through separate columns on a vacuum manifold to condense phytoplankton biomass on GF/Fs. Pigment samples were stored (−20 °C) in plastic scintillation vials until acetone extraction (with 90% HPLC grade acetone) of chl-*a* concentrations (μg L^{-1}) using a Turner Trilogy® fluorometer (Welschmeyer 1994). For each sample, the >20 μm cell size fraction was calculated by subtracting <20 μm chl-*a* concentrations from total chl-*a*, and 5–20 μm was calculated by subtracting the >20 and < 5 μm concentrations from total chl-*a*.

2.3.3. Phytoplankton community composition

One replicate (chosen at random) per site or treatment was qualitatively analyzed for community composition using a 5 mL Lab-Tek™ Chamber Slide with all visible species identified to the lowest taxonomic level (LTL) possible. Additionally, 20 mL aliquots per replicate were dispensed into 20 mL glass amber vials, fixed with Lugol's iodine solution (Sigma-Aldrich® product #1.00567) to a 1% final dilution, then refrigerated (4 °C) until analysis. To quantify phytoplankton community composition, all preserved samples were evaluated using an Olympus CKX53 inverted light microscope and a 1 mL Sedgewick-Rafter chamber. Individual cells (nano- and microplankton) were identified to the LTL possible then enumerated until 300 cells per species or the entire chamber was counted, whichever occurred first. Cell concentrations were calculated using the following equation (LeGresley and McDermott 2010):

$$\frac{counted\ cells}{1\ mL} * \frac{mL\ sample\ and\ Lugols\ iodine\ solution}{mL\ total\ sample}$$

2.4. Statistical analysis

All data were tested for normality (Shapiro-Wilk) prior to analyses. Chl-*a* and DIN concentrations did not satisfy parametric assumptions and were subsequently analyzed using non-parametric tests. Bioassay cell count growth rates met parametric assumptions and were analyzed as below. R Studio (v1.4.1106) was used for all tests with a significance level of $\alpha = 0.05$.

For nearshore sampling, the relationship of chl-*a* to physical water quality (T, S, DO, turbidity, and pH) and inorganic nutrient concentrations (AmN, N + N, DIP, and Si) was tested using a Spearman rank correlation per site. The relationships of AmN and N + N to physical water quality and chl-*a* cell size fractions, as well as precipitation to physical water quality, nutrient concentrations, and total chl-*a,* were tested similarly. For bioassays, differences in chl-*a* (total and per cell size fraction) between t (0) and each treatment at t (24) were compared using Wilcoxon rank sum tests. Significant differences in mean chl-*a* concentrations (total and cell size fractions), cell abundances, and chl-*a* growth rates (between all timepoints) were determined among treatments using a Kruskal-Wallis chi squared test followed by Dunn's test of multiple comparisons with a Bejamini-Hochberg adjustment. Phytoplankton cell growth rates were tested among treatments using a one-way analysis of variance (ANOVA) followed by a Tukey-post hoc test. Significant differences among nutrient uptake rates per treatment were likewise assessed using a Kruskal-Wallis chi squared test.

3. Results

3.1. Field surveys

3.1.1. Physical water quality

At all shore sites, mean (±SE, and similar notation henceforth) temperature (T, 12.20 ± 0.91 °C) was similar between sites on a given day but fluctuated seasonally with July 2021 the warmest month and Feb. 2021 the coolest (Fig. 2a). Salinity (S) was comparable among CI, RP, and CP for all dates (pooled mean 28.4 ± 0.30 PSU), but more variable at AC and SR (pooled mean 19.5 ± 1.17 PSU; Fig. 2b). The lowest value (3.77 PSU, 03 Sept. 2021) at SR followed intense rainfall (7-day sum at Norwalk 88.9 mm; Table S2) and coincided with elevated turbidity (14.78 FNU) and nitrate + nitrite (N + N, 12.50 ± 0.23 μM; Figs. 2 and 3). Dissolved oxygen (DO) across sites (pooled mean 8.95 ± 0.29 mg L^{-1}) was lowest during Aug. and Sept. 2021, reaching a 2.46 mg L^{-1} minimum on 03 Sept. 2021 at AC, indicative of hypoxia (DO < 3.0 mg L^{-1}; CT-DEEP 2021, Fig. 2c). The two sites closest to WW inputs, AC and SR, were generally more turbid (pooled mean 12.13 ± 2.94 FNU; Fig. 2d) than CI, RP, or CP (pooled mean 1.97 ± 0.82 FNU); however, precipitation was only significantly associated with turbidity at RP (Spearman rank coefficient, henceforth r, = 0.55, p = 0.04; Table S3) and not significantly correlated with T, S, DO, pH, total chl-*a*, ammonia-N (AmN), N + N, PO_4^{3-} (DIP), or SiO_4^{4-} (Si) across sites. Finally, waters at AC were more acidic (mean pH 7.48 ± 0.09) than other sites (pooled mean pH 7.88 ± 0.03; Fig. 2e).

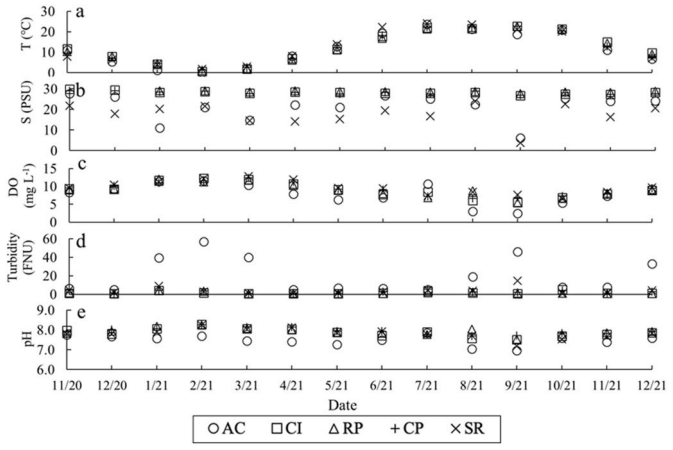

Fig. 2. Time series (mm/yy) of physical water quality at shore sites during the study period. Parameters include water a) temperature (T, °C), b) salinity (S, PSU), c) dissolved oxygen (DO, mg L^{-1}), d) turbidity (FNU), and e) pH. Site abbreviations are as in Fig. 1.

3.1.2. Nutrients

Mean N + N concentrations at AC (24.29 ± 3.93 μM) and SR (12.64 ± 3.21 μM) were higher than other sites (pooled mean 3.18 ± 1.07 μM; Fig. 3a–e). Lowest concentrations were recorded at CP (mean 1.89 μM ± 0.50 μM: Fig. 3c), with minima and maxima not coincident across sites. In 2021, N + N values were elevated at AC (60.93 ± 1.42 μM on 07 Jan.) and CI (43.16 ± 0.27 μM on 21 Oct.). N + N was positively correlated with Si at CI, RP, and CP ($r = 0.76$, 0.59, and 0.54, $p < 0.01$, 0.02, and 0.04, respectively) but not correlated with other variables across sites, with the exception of AmN at RP ($r = 0.66$, $p = 0.01$).

Mean AmN concentrations at AC (10.33 ± 2.15 μM; Fig. 3a) were higher than other sites (pooled mean 2.12 ± 0.37 μM), reaching 21.96 ± 0.70 μM on Nov. 05, 2021. Across sites, AmN concentrations rose during late fall (20 Nov., Dec. 11, 2020, and Dec. 3, 2021) when chl-*a* declined (Figs. 3 and 4). The lowest AmN values were at RP (mean 1.20 ± 0.42 μM; Fig. 3c) and during late winter across sites (Mar. 08, 2021), but late winter AmN declines did not coincide with changes in chl-*a* levels. AmN was negatively and significantly correlated with T at AC ($r = -0.60$, $p = 0.02$) but not with other parameters across sites.

Mean concentrations of DIP generally decreased along the urban-suburban gradient such that AC (3.49 ± 0.09 μM) had consistently higher values than SR (1.31 ± 0.22 μM) (Fig. 3f–j). The highest DIP value (6.69 ± 0.53 μM) on Oct. 04, 2021 at AC coincided with a mixed phytoplankton species bloom of *Prorocentrum minimum* (3087 ± 250 cells mL^{-1}), euglenoids (2590 ± 43 cells mL^{-1}), and *Thalassiosira* spp. (1619 ± 427 cells mL^{-1}; Table S4). Minima were not coincident among sites, but apart from AC all sites reached their maxima on Nov. 20, 2020. DIP was not significantly correlated with chl-*a* or precipitation across sites (Table 1, Table S3).

There were no distinct spatial gradients in Si (Fig. 3f–j). Temporally, highest Si concentrations occurred late summer/fall 2021 at all sites except AC, which reached 22.53 ± 0.67 μM on Mar. 08, 2021, along with elevated N + N but not chl-*a*. March 2021 Si decreases occurred across sites, dropping to 0.01 ± 0.00 μM on Mar. 08, 2021 at CI, when the diatom *Skeletonema* spp. was abundant (3964 ± 792, 2664 ± 235, 1421 ± 144, 6571 ± 534, and 2451 ± 736 cells mL^{-1} at AC, CI, RP, CP and SR, respectively), indicating draw-down. Across sites, Si was positively, though not significantly, correlated with total chl-*a* (Table 1), had no consistent associations with AmN, but negatively and significantly correlated with DO ($r = -0.75$, $p = <0.01$) and pH ($r = -0.85$, $p = <0.01$) at CI.

3.1.3. Chl-a

Across sites, total chl-*a* concentrations peaked during summer 2021 (July and Aug.) and were minimal during Nov. (2020 and 2021; Fig. 4). Mean total chl-*a* was higher at AC (24.72 ± 13.62 μg L^{-1}) than other sites (pooled mean 6.58 ± 1.14 μg L^{-1}) and negatively correlated with AmN; this was significant at AC ($r = -0.77$, $p < 0.01$) and CP ($r = -0.63$, $p = 0.02$; Table 1). Total chl-*a* positively correlated with turbidity and T at all sites, and this was significant for turbidity at RP ($r = 0.56$, $p = 0.04$) and T at SR ($r = 0.58$, $p = 0.03$). Chl-*a* was negatively correlated with N + N, pH, and DO, with the latter significant at SR ($r = -0.55$, $p = 0.04$). There were no clear associations between either DIP or Si and chl-*a*.

The greatest proportion of microplankton (>20 μm) to overall phytoplankton biomass occurred in winter 2021 at CI, RP, and CP (Fig. 4) reaching 8.78 ± 1.14 μg L^{-1} (68% of total chl-*a*) and 12.61 ± 0.99 μg L^{-1} (74%), at CI and RP, respectively, on Jan. 07, 2021 and 3.91 ± 0.21 μg L^{-1} (74%) at CP on Mar. 08, 2021. These winter assemblages were primarily composed of the chain forming diatoms *Skeletonema* spp. and *Thalassiosira* spp. although other species likely contributed chl-*a* to this size fraction. Microplankton biomass maxima occurred at AC on Oct. 04, 2021 (26.47 ± 5.66 μg L^{-1}, 34% of biomass) along with a mixed diatom and flagellate bloom dominated by the HAB species *P. minimum* at 3087 ± 250 cells mL^{-1} (Table S4) and at SR on Aug. 05, 2021 (12.25 ± 3.52 μg L^{-1}, 50% of biomass). Microplankton chl-*a* concentrations

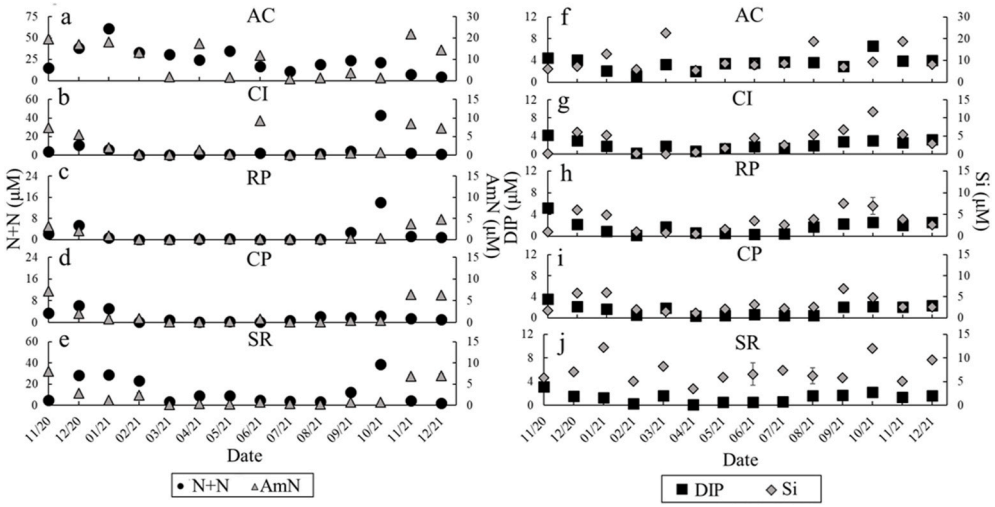

Fig. 3. Mean ($n = 3$) ± SE nutrient concentrations (μM) per sampling date (mm/yy) for $NO_3^- + NO_2^-$ (N + N), primary axis and NH_3+NH_4^+ (AmN), secondary axis at a) AC, b) CI, c) RP, d) CP, and e) SR. Also shown are PO_4^{3-} (DIP) and SiO_4^{4-} (Si) at f) AC, g) CI, h) RP, i) CP, and j) SR. Site abbreviations are as in Fig. 1.

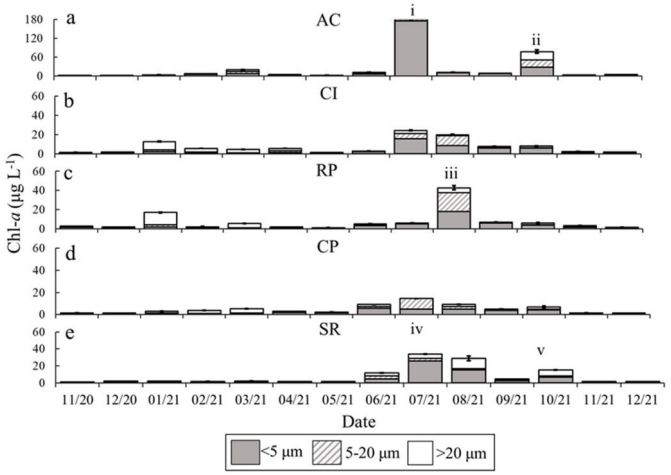

Fig. 4. Mean ($n = 3$) ± SE chl-*a* concentrations per sampling date (mm/yy) at a) AC b) CI c) RP d) CP and e) SR. Chl-*a* cell size fractions (<5 μm, 5–20 μm, and >20 μm) displayed as contributions to total chl-*a*. Error bars represent SE for mean total chl-*a*. Note difference in y-axes. Notable HAB and other flagellate blooms are denoted as i) July 08, 2021 at AC ii) 04 Oct. 21 at AC iii) 05 Aug. 21 at RP iv) 08 July 21 at SR and v) Oct. 04, 2021 at SR. Blooms are detailed in Table S4. Site abbreviations are as in Fig. 1.

negatively correlated with AmN across sites, and this was significant at AC ($r = -0.86$, $p = <0.01$), CI ($r = -0.61$, $p = 0.02$) and SR ($r = -0.63$, $p = 0.02$; Table S5).

Chl-*a* maxima of nanoplankton (5–20 μm cell size fraction) were observed summer 2021 at CI (05 Aug., 10.03 ± 0.80 μg L^{-1}, 51 % of biomass), RP (05 Aug., 19.74 ± 2.22 μg L^{-1}, 51% of biomass), CP (08 July, 9.43 ± 9.01 μg L^{-1}, 49% of biomass), and SR (07 June, 3.54 ± 0.48 μg L^{-1}, 31% of biomass) but in fall 2021 at AC (04 Oct., 23.58 ± 5.65 μg L^{-1}, 31% of biomass; Fig. 4). These events coincided with flagellate blooms, including *Prorocentrum triestinum* (5257 ± 81 cells mL^{-1}) at RP on Aug. 05, 2021 (Table S4). Minima were observed across sites on May 07, 2021 (Fig. 4). Nanoplankton chl-*a* concentrations were negatively correlated with AmN at AC, CI, CP, and SR; this was significant at CP ($r = -0.64$, $p = 0.01$; Table S5).

The greatest contributions of picoplankton and small nanoplankton (<5 μm) to total phytoplankton biomass occurred during summer 2021 across sites (Fig. 4). On 08 July, chl-*a* was dominated by the <5 μm cell size fraction, coinciding with peak T (21.3–24.0 °C). On this occasion, picoplankton and small nanoplankton at AC contributed 175.88 ± 9.35 μg L^{-1} (93.5%) to total chl-*a* when *Heterocapsa* spp. (4131 ± 913 cells mL^{-1}) and euglenoids (2485 ± 217 cells mL^{-1}) bloomed (Table S4). Phytoplankton biomass (<5 μm) was higher at AC (mean 18.26 ± 6.93 μg L^{-1}) than other sites (pooled mean 3.42 ± 0.38 μg L^{-1}) and negatively correlated with AmN concentrations at AC, CI, CP, and SR; this was significant at AC ($r = -0.77$, $p < 0.01$; Table S5).

3.1.4. Phytoplankton community composition

Diatoms, particularly *Thalassiosira* spp. and *Skeletonema* spp., were the numerically dominant winter taxon at all sites. Blooms of *Thalassiosira* spp. (2035 ± 101 and 1411 ± 104 cells mL^{-1}) and *Skeletonema* spp. (11,250 ± 4692 and 12,563 ± 500 cells mL^{-1}) were observed at RP and CI, respectively, on Jan. 07, 2021 when N + N concentrations were 0.75 ± 0.02 and 6.15 ± 0.04 μM. Diatom predominance across sites continued into late winter and spring 2021, with *Heterocapsa* sp. and cryptophytes the only regularly-observed flagellates. For example, during the Mar. 08, 2021 *Skeletonema* spp. bloom, numerous *Thalassiosira* spp. (426 ± 57 cells mL^{-1}), *Heterocapsa* sp. (177 ± 47 cells mL^{-1}), and cryptophytes (70 ± 19 cells mL^{-1}) occurred with elevated N + N concentrations (30.62 ± 1.57 μM) at AC (Fig. 3). Precipitation was minimal before this date (4.05 mm 7-day sum; Table S2).

Summer 2021 phytoplankton assemblages were more taxonomically diverse, with numerous dinoflagellates, cryptophytes, and euglenoids, including HAB species (Table S4). On 08 July, the mixed flagellate and picoplankton bloom at AC coincided with low AmN, the warmest study T (Table S4), and a similar assemblage at SR (*Heterocapsa* spp. 1232 ± 95 cells mL^{-1} and euglenoids 246 ± 8 cells mL^{-1}). On 05 Aug., a mixed species dinoflagellate bloom at RP included *P. triestinum* (5257 ± 81 cells mL^{-1}), *P. minimum* (1076 ± 142 cells mL^{-1}), and *Gymnodinium* spp. (1005 ± 135 cells mL^{-1}) following a period of low rainfall (9.91 mm 7-day sum; Table S2) with low DIN. Mixed assemblages continued into fall: on Oct. 04, 2021, high concentrations of flagellates, including a dense bloom of *P. minimum* (3087 ± 250 cells mL^{-1}) alongside euglenoids (2590 ± 43 cells mL^{-1}) and *Thalassiosira* spp. (1619 ± 427 cells mL^{-1}), were observed at AC (Table S4).

3.2. In situ bioassays

Throughout experiments, T, pH and *k* were comparable across sites, but TG had higher S and lower DO (Table 2). Initial (t0) DIN concentrations were lower than historical values at both sites (Table 3, Table S1) with TG having lower N + N levels (4.43 ± 0.08 μM on 07 Sept. 2021) than SR (5.18 ± 0.19 μM on 14 Sept. 2021) but higher AmN (7.16 ± 0.28 compared to 6.70 ± 0.15 μM) (Table 3, Table S1). Total t (0) chl-*a* at TG and SR was 4.47 ± 0.02 and 5.88 ± 0.20 μg L^{-1}, respectively, with TG biomass including less of the <5 μm cell size fraction (2.49 ± 0.02 versus 4.87 ± 0.21 μg L^{-1} chl-*a*; Fig. 5).

At t (24), there were no significant differences in total biomass among treatments at TG (Kruskal-Wallace H (5) = 5.23, $p = 0.38$) or SR

Table 2
Physical water quality for T (°C), Salinity (S), Turbidity (FNU), DO (mg L^{-1}), pH, and Secchi depth (m) at each time point (t (0), t (24), t (72)) during the course of each bioassay experiment. The light extinction coefficient (*k*) was calculated from the Secchi depth (Brown 1984). Sites are abbreviated as Throggs Neck (TG) and Saugatuck River (SR). "–" indicates that measurements were not available.

Date (2021)	Site	Time Point	T	S	DO	pH	Secchi Depth	*k*
07 Sep.	TG	t (0)	24.0	24.2	5.03	8.16	1.5	1.13
08 Sep.	TG	t (24)	–	–	–	–	1.5	1.13
10 Sep.	TG	t (72)	23.3	24.6	4.78	–	1.5	1.13
14 Sep.	SR	t (0)	23.0	17.8	5.70	8.14	1.6	1.06
15 Sep.	SR	t (24)	24.0	19.6	6.96	8.12	1.4	1.21
17 Sep.	SR	t (72)	23.7	23.8	6.36	8.30	1.4	1.21

Table 1
Spearman's rank correlation coefficients (*r*) for AmN, N + N, DIP, Si (all μM), T (°C), Salinity (S), Turbidity (FNU), DO (mg L^{-1}), and pH according to total chl-*a* concentrations (μg L^{-1}) throughout the study period. Sites are abbreviated as Fig. 1. Significance (95% confidence, α = 0.05) is expressed for each coefficient as **bold** = 0.05, **(bold)*** = 0.01, and **(bold)**** = 00.

Site	AmN	N + N	DIP	Si	T	S	Turbidity	DO	pH
AC	**−0.78****	−0.24	−0.08	0.32	0.45	−0.09	0.25	−0.09	−0.02
CI	−0.51	−0.06	−0.27	0.19	0.34	−0.42	0.52	−0.25	−0.05
RP	−0.13	−0.03	0.05	0.21	0.45	−0.41	**0.56**	−0.23	−0.13
CP	**−0.63***	−0.27	−0.48	0.12	0.43	−0.09	0.10	−0.42	−0.29
SR	−0.41	−0.11	0.13	0.21	**0.58**	0.24	0.16	**−0.55**	−0.30

(Kruskal-Wallace H (5) = 8.84, $p = 0.16$; Fig. 5), and growth rates (t (0)-t (24)) were also not significantly different between treatments in either experiment. At t (72), there were no significant differences in total biomass among treatments at TG (Kruskal-Wallace H (5) = 2.51, $p = 0.77$) or SR (Kruskal-Wallace H (5) = 7.89, $p = 0.16$). Growth rates were not significantly different between treatments in either experiment for (t (0)-t (72)) at TG. However, at SR growth rates (t (24)-t (72)) were significantly different (Kruskal-Wallace H (5) = 11.27, $p = 0.05$) such that phytoplankton in the ALL treatment grew more rapidly than NP or UP (Dunn post-hoc, $p < 0.01$ and 0.01), and P phytoplankton grew faster than NP (Dunn post-hoc, $p = 0.03$). There were no significant differences at any timepoint for cell size fraction biomasses or growth rates between treatments in either experiment.

In both experiments, N + N decreased dramatically compared to AmN (Table 3), indicating N + N draw-down. DON was highest in NP at both TG timepoints, while at SR DON was highest at t (24) in C and at t (72) in UP. DIN:DIP was lowest across experiments and timepoints in P, highest in AP at TG for both timepoints, and highest at SR t (24) in AP and t (72) in C. At t (72), Si was lowest in UP at TG but in NP at SR, though Si:DIN was lowest in AP at both sites. V_{N+N} (all rates t (24)-t (72)) was not significantly different between treatments at TG (Table S6), but was at SR (Kruskal-Wallace H (5) = 12.35, $p = 0.03$; Table S6), with higher rates in ALL than C ($p = 0.02$, Dunn post-hoc). V_{AmN} differed significantly between treatments at TG (Kruskal-Wallace H (5) = 11.25, $p = 0.05$), with lower uptake in ALL than C ($p = 0.01$ Dunn post-hoc), and it also differed significantly at SR (Kruskal-Wallace H (5) = 12.15, $p = 0.03$) with higher uptake in C than either AP ($p < 0.01$ Dunn post-hoc) or UP ($p = 0.04$ Dunn post-hoc). There were no significant differences in V_{DIP} or V_{Si} (Table S6).

Similar to field surveys, diatoms were the most abundant phytoplankton taxa during experiments, with *Thalassiosira* spp. and *Skeletonema* spp. among the most common genera as well as *Lithodesmium* sp. at TG and *Leptocylindrus* sp. at SR (Fig. 6). Diatom abundances rose in all treatments during experiments, and although cell abundances between treatments were not significantly different at any given time point, cell numbers increased in NP and AP at TG and ALL at SR. Growth rates (t (24)-t (72)) at TG were fastest for *Skeletonema* spp., *Thalassiosira* spp., and *Lithodesmium* spp. in NP, while at SR diatom growth was not consistently elevated with any nutrient addition (Table S7).

Generally, flagellate counts were low during bioassays (Table S8). At TG, there were few dinoflagellates and euglenoid abundances were minimal (2 ± 1 cells mL^{-1}). Cryptophytes, however, were abundant (249 ± 9 cells mL^{-1}) and most numerous in the t (72) AP treatment (46 ± 22 cells mL^{-1}), coincident with fastest growth ((t (24)-t (72); Table S7). Across treatments, there were significant differences in t (24) TG cryptophyte abundances (Kruskal-Wallace H (5) = 13.47, $p = 0.02$), with fewer cells in ALL than UP (Dunn post-hoc $p = 0.01$), as well as growth rates (t (0)-t (24), 1-way ANOVA, F (5,11 = [13.4], $p < 0.01$), though ALL and UP growth rates were faster than C ($p = 0.02$, 95% Confidence Interval, CI = [0.002–0.047]) and ($p = 0.02$, 95% CI = [0.003–0.048]), respectively. At SR, few dinoflagellates were observed but euglenoids were initially abundant (499 ± 57 cells mL^{-1}); by t (72) flagellate abundances decreased most in NP, though this decline was not statistically significant. Positive euglenoid growth (t (24)-t (72)), was only observed in AP (Table S7). Unlike TG, cryptophytes were not initially abundant at SR (45 ± 10 cells mL^{-1}), and from t (24)-t (72) they only exhibited positive growth in P and AP (Table S7). Differences in growth rates were noted for certain diatoms at SR. As examples, across treatments, *Cerataulina* sp. abundances were significantly different at t (72) (Kruskal-Wallace H (5) = 12.86, $p = 0.02$), though a Dunn-post hoc was not significant. Growth rates (t (0)-t (72)) were significantly different for *Chaetoceros* spp. (1-way ANOVA, F (5,12 = [3.251], $p = 0.04$), though a Tukey-post hoc was not significant and for *Cylindrotheca closterium* betweewn treatments (t (0)-t (24), F (5,12 = [3.87], $p = 0.03$), with ALL exhibiting faster growth than C ($p = 0.05$, 95% CI = [−1.038 to −0.005]).

4. Discussion

This research showed that low N + N with minimal shifts in AmN and DON following COVID-19 SIP likely impacted the relative abundances of diatom and flagellate species within WLIS (and potentially other urban estuaries). Throughout this study, and consistent with pre-COVID patterns, overall DIN concentrations generally declined with distance from the NYC metropolitan area with the exception of sites adjacent to WW inputs. Phytoplankton assemblages were primarily composed of diatoms, though cryptophytes, euglenoids, and mixotrophic dinoflagellates, such as *Heterocapsa* spp., were common, along with summer *Prorocentrum* spp. blooms. Shore surveys and bioassays identified taxonomic responses to DIN-form, with N + N increasing diatom concentrations relative to cryptophyte and euglenoid growth and AmN having an inhibitory effect. Conversely, euglenoids and crytophytes were more abundant when N + N was low, with cryptophytes exhibiting a preference for AmN. These findings indicate that lower total DIN concentrations during COVID-19 SIP may have modified phytoplankton community composition, and potentially estuarine DIN:DON, despite

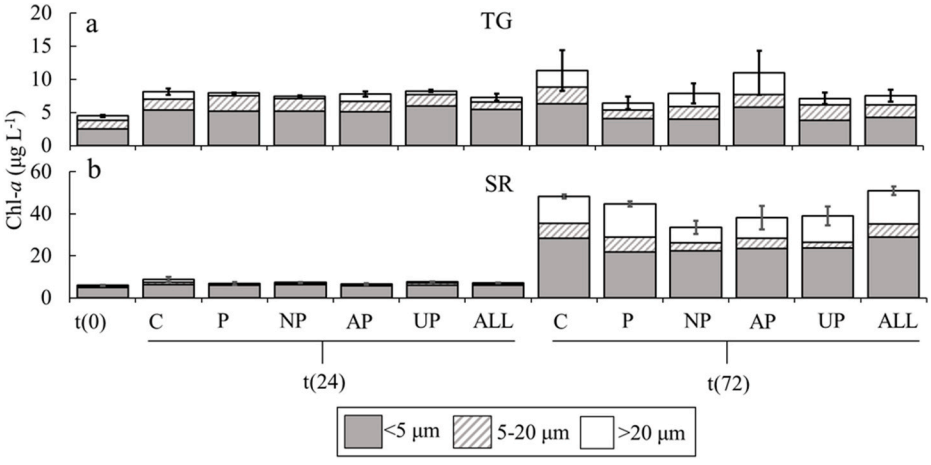

Fig. 5. Mean ($n = 3$) ± SE chl-*a* concentrations per bioassay treatment at timepoints t (0), t (24) and t (72) at a) TG and b) SR. Chl-*a* cell size fractions (<5 µm, 5–20 µm, and >20 µm) are displayed as contributions to total chl-*a*. Error bars represent SE for mean total chl-*a*. Note differences in y-axes. Sites are abbreviated as in Fig. 1. Addition treatments are noted as C=Control, P=Phosphate, NP=Nitrate and Phosphate, AP=Ammonium and Phosphate, UP=Urea and Phosphate, ALL = ALL nutrient forms.

Table 3
Mean ($n = 3$) ± SE inorganic nutrient concentrations (μM) in each bioassay experiment across all treatments. Nutrient addition and site abbreviations are as in Fig. 5. "-" indicates measurements were not available/applicable.

Site	Timepoint	Nutrient	Initial Condition	C	P	NP	AP	UP	ALL
TG	**t(0)**	N + N	4.43 ± 0.08	–	-	-	-	-	-
		AmN	7.16 ± 0.28	–	-	-	-	-	-
		DIN	11.58 ± 0.29	–	-	-	-	-	-
		TDN	34.36 ± 1.27	–	-	-	-	-	-
		DON	22.77 ± 1.30	–	-	-	-	-	-
		Si	6.73 ± 0.11	–	-	-	-	-	-
		DIP	4.88 ± 0.26	–	-	-	-	-	-
		TDP	4.63 ± 0.16	–	-	-	-	-	-
		DOP	0.06 ± 0.00	–	-	-	-	-	-
		DIN:DIP	2.39 ± 0.07	–	-	-	-	-	-
		DON:DOP	352.54 ± 0.27	–	-	-	-	-	-
		Si:DIN	0.58 ± 0.02	–	-	-	-	-	-
	t(24)	N + N	–	4.75 ± 0.04	4.87 ± 0.06	13.30 ± 0.17	3.94 ± 0.46	4.45 ± 0.12	6.68 ± 0.27
		AmN	–	4.53 ± 0.10	4.26 ± 0.26	5.17 ± 0.26	26.10 ± 0.91	4.01 ± 0.16	10.49 ± 0.27
		DIN	–	9.28 ± 0.29	9.13 ± 0.26	18.47 ± 0.31	30.05 ± 1.02	8.46 ± 0.20	17.17 ± 0.38
		TDN	–	42.64 ± 1.82	56.70 ± 2.14	115.87 ± 1.32	87.32 ± 1.45	80.89 ± 2.11	83.99 ± 3.96
		DON	–	33.36 ± 1.70	47.56 ± 2.04	97.40 ± 1.59	57.27 ± 0.74	72.44 ± 2.19	66.82 ± 4.37
		Si	–	4.44 ± 0.09	5.92 ± 0.15	4.53 ± 0.13	4.63 ± 0.17	3.58 ± 0.14	5.05 ± 0.11
		DIP	–	4.14 ± 0.11	7.11 ± 0.21	6.37 ± 0.18	6.07 ± 0.07	5.76 ± 0.25	5.52 ± 0.32
		TDP	–	4.24 ± 0.05	6.13 ± 0.20	6.39 ± 0.10	5.95 ± 0.21	6.00 ± 0.08	6.00 ± 0.11
		DOP	–	0.14 ± 0.08	0.06 ± 0.00	0.22 ± 0.09	0.18 ± 0.12	0.31 ± 0.19	0.61 ± 0.28
		DIN:DIP		2.24 ± 0.06	1.29 ± 0.07	2.9 ± 0.14	4.95 ± 0.32	1.48 ± 0.11	3.12 ± 0.12
		DON:DOP	–	369.52 ± 0.36	736.28 ± 0.30	746.79 ± 0.26	630.93 ± 0.29	525.50 ± 0.42	363.87 ± 0.64
		Si:DIN	–	0.48 ± 0.01	0.65 ± 0.03	0.25 ± 0.01	0.14 ± 0.01	0.42 ± 0.02	0.29 ± 0.01
	t(72)	N + N	–	2.41 ± 0.19	2.36 ± 0.21	5.95 ± 0.23	2.66 ± 0.05	2.43 ± 0.14	2.56 ± 0.15
		AmN	–	1.86 ± 0.27	3.70 ± 0.33	2.51 ± 0.04	25.27 ± 0.70	2.75 ± 0.20	10.18 ± 0.13
		DIN	–	4.27 ± 0.33	6.06 ± 0.39	8.49 ± 0.23	27.93 ± 0.70	5.18 ± 0.25	12.73 ± 0.20
		TDN	–	33.64 ± 2.34	45.87 ± 3.64	80.66 ± 3.52	64.55 ± 4.47	68.40 ± 5.21	58.96 ± 2.61
		DON	–	29.37 ± 2.33	39.81 ± 3.57	72.17 ± 3.24	36.62 ± 4.79	63.22 ± 5.12	46.21 ± 2.45
		Si	–	7.09 ± 0.05	7.68 ± 0.65	7.60 ± 0.06	7.11 ± 0.33	5.78 ± 0.04	6.78 ± 0.18
		DIP	–	2.33 ± 0.05	5.56 ± 0.37	4.78 ± 0.33	5.06 ± 0.51	4.35 ± 0.13	4.05 ± 0.33
		TDP	–	3.98 ± 0.14	5.23 ± 0.31	5.35 ± 0.17	4.97 ± 0.15	5.44 ± 0.17	4.75 ± 0.15
		DOP	–	1.65 ± 0.12	0.09 ± 0.02	0.57 ± 0.25	0.38 ± 0.31	1.09 ± 0.21	0.70 ± 0.33
		DIN:DIP		1.83 ± 0.05	1.10 ± 0.11	1.79 ± 0.08	5.67 ± 0.23	1.19 ± 0.05	3.19 ± 0.10
		DON:DOP	–	17.98 ± 0.44	496.20 ± 0.57	311.57 ± 0.51	430.46 ± 0.94	60.62 ± 0.67	458.06 ± 0.54
		Si:DIN	–	1.66 ± 0.13	1.27 ± 0.14	0.90 ± 0.03	0.25 ± 0.01	1.12 ± 0.05	0.53 ± 0.02
SR	**t(0)**	N + N	5.18 ± 0.19	–	-	-	-	-	-
		AmN	6.70 ± 0.15	–	-	-	-	-	-
		DIN	11.89 ± 0.24	–	-	-	-	-	-
		TDN	94.46 ± 5.22	–	-	-	-	-	-
		DON	82.57 ± 0.01	–	-	-	-	-	-
		Si	5.61 ± 0.79	–	-	-	-	-	-
		DIP	3.25 ± 0.28	–	-	-	-	-	-
		TDP	2.71 ± 0.18	–	-	-	-	-	-
		DOP	0.09 ± 0.02	–	-	-	-	-	-
		DIN:DIP	3.70 ± 0.31	–	-	-	-	-	-
		DON:DOP	1028.66 ± 0.58	–	-	-	-	-	-
		Si:DIN	0.47 ± 0.07	–	-	-	-	-	-
	t(24)	N + N	–	3.37 ± 0.02	3.42 ± 0.01	9.37 ± 0.26	5.44 ± 0.27	4.40 ± 0.12	8.71 ± 0.22
		AmN	–	3.62 ± 0.63	5.46 ± 0.26	4.73 ± 0.30	25.72 ± 0.20	6.87 ± 0.24	14.32 ± 0.67
		DIN	–	6.99 ± 0.63	8.88 ± 0.26	14.10 ± 0.40	31.16 ± 0.34	11.27 ± 0.27	23.03 ± 0.71
		TDN	–	66.95 ± 0.93	41.76 ± 4.51	68.78 ± 1.76	62.65 ± 2.90	68.07 ± 3.82	64.88 ± 2.91
		DON	–	59.96 ± 1.09	32.87 ± 4.76	54.68 ± 1.97	31.49 ± 2.94	56.80 ± 3.56	41.85 ± 3.76
		Si	–	14.74 ± 0.15	16.24 ± 0.09	15.23 ± 0.12	14.26 ± 0.14	13.92 ± 0.57	13.95 ± 1.10
		DIP	–	2.38 ± 0.03	4.41 ± 0.03	4.33 ± 0.02	4.11 ± 0.11	4.03 ± 0.09	4.42 ± 0.10
		TDP	–	3.70 ± 0.49	3.63 ± 0.08	3.98 ± 0.11	3.67 ± 0.02	3.66 ± 0.23	3.75 ± 0.13
		DOP	–	1.33 ± 0.52	0.06 ± 0.00	0.06 ± 0.00	0.06 ± 0.00	0.05 ± 0.01	0.06 ± 0.00
		DIN:DIP	–	2.95 ± 0.04	2.02 ± 0.02	3.26 ± 0.03	7.59 ± 004	2.80 ± 0.04	5.21 ± 0.14
		DON:DOP	–	79.64 ± 0.47	508.85 ± 0.83	846.44 ± 0.27	487.44 ± 0.52	1172.36 ± 0.48	647.85 ± 0.58
		Si:DIN	–	2.14 ± 0.19	1.83 ± 0.05	1.08 ± 0.03	0.46 ± 0.01	1.24 ± 0.06	0.60 ± 0.05
	t(72)	N + N	–	2.15 ± 0.19	2.56 ± 0.15	7.61 ± 0.14	3.46 ± 0.11	3.44 ± 0.02	5.04 ± 0.04
		AmN	–	2.66 ± 0.27	4.21 ± 0.28	3.72 ± 0.20	16.73 ± 0.48	3.61 ± 0.24	13.31 ± 0.73
		DIN	–	4.81 ± 0.33	6.77 ± 0.32	11.34 ± 0.25	20.19 ± 0.49	7.05 ± 0.24	18.35 ± 0.74
		TDN	–	5.40 ± 0.29	35.50 ± 2.39	60.15 ± 4.41	62.76 ± 3.14	56.94 ± 1.76	60.03 ± 0.71
		DON	–	0.73 ± 0.36	28.73 ± 2.54	48.81 ± 4.45	42.58 ± 3.31	49.89 ± 1.78	42.06 ± 1.81
		Si	–	13.15 ± 0.76	13.82 ± 0.42	9.64 ± 1.57	11.40 ± 0.90	14.09 ± 0.20	12.61 ± 0.41
		DIP	–	0.47 ± 0.06	2.80 ± 0.10	3.18 ± 0.14	2.85 ± 0.05	2.80 ± 0.26	2.53 ± 0.09
		TDP	–	1.24 ± 0.04	2.45 ± 0.11	3.49 ± 0.19	2.98 ± 0.16	2.71 ± 0.30	2.58 ± 0.17
		DOP	–	0.77 ± 0.09	0.06 ± 0.00	0.31 ± 0.13	0.17 ± 0.11	0.04 ± 0.02	0.19 ± 0.13
		DIN:DIP	–	10.51 ± 0.13	2.43 ± 0.05	3.58 ± 0.20	7.08 ± 0.15	2.56 ± 0.09	7.25 ± 0.08
		DON:DOP	–	0.89 ± 0.44	444.75 ± 0.47	202.19 ± 0.68	471.15 ± 0.57	5506.49 ± 0.27	651.13 ± 0.45
		Si:DIN	–	2.76 ± 0.24	2.05 ± 0.11	0.85 ± 0.14	0.57 ± 0.05	2.00 ± 0.07	0.69 ± 0.04

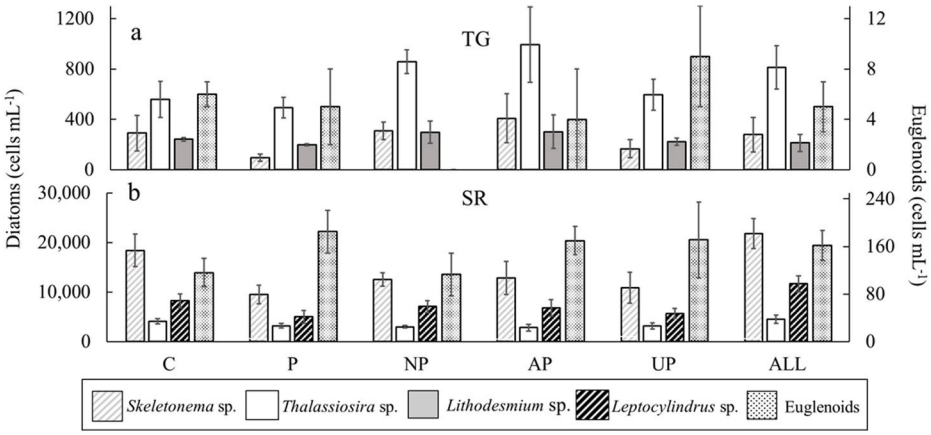

Fig. 6. Mean (n = 3) ± SE cell concentrations at t (72) for the most abundant diatom genera as well as euglenoids for each bioassay. Note difference in y-axis. Nutrient additions and site abbreviations are as in Fig. 5.

transient influences on total phytoplankton biomass. LIS management should therefore consider the ecological impact of N-form delivered by wastewater in addition to the bulk N pool.

Physical water quality conditions among CI, RP, and CP were comparable to offshore in the WLIS mainstem (CT-DEEP 2021; Humphries et al., 2023; Roldan-Ayala et al., 2023). T was consistent across sites while DO concentrations increased moving away from the urbanized Narrows. DO fluctuated seasonally with lower values during warmer months, consistent with oxygen solubility declining as T rises. Hypoxic conditions at AC were likely due to intensified microbial respiration of CSO nutrients (Miskewitz and Uchrin 2013). The comparatively lower S at AC and SR was presumably due to terrestrial and riverine inputs. Elevated turbidity at AC may have been caused by tidal resuspension of particulate and organic matter because it was not correlated with precipitation whereas at SR the positive correlation between turbidity and precipitation suggested greater sediment loading in runoff vs. distance from NYC; notably, SR precipitation was not correlated with DIN.

Unlike offshore (Suter et al., 2014; Roldan-Ayala et al., 2023), shore N + N concentrations did not exhibit a decreasing urban-suburban gradient as CP exhibited the lowest mean value while SR had the second highest. N + N concentrations at AC and SR reached an order of magnitude greater than offshore on several dates whereas CI and RP concentrations were rarely high (Humphries et al., 2023). Since WW effluent contains up to ~30 mg L^{-1} N + N (~2100 μM; EPA, 2012), elevated N + N at AC and SR compared to other sites suggests they were enriched by nearby WW inputs. Alternatively, since N + N can be elevated in lakes and ponds near golf courses (Mallin et al., 2016; Reed et al., 2016; Bock and Easton 2020), which both AC and SR are adjacent to, some of this excess N + N could have originated from fertilizers. CI, RP, and CP exhibited similar concentration ranges to Chesapeake Bay (0.05–9 μM N + N; Egerton et al., 2014; Morse et al., 2014) and Buzzards Bay (1–3 μM N + N; Turner et al., 2000), suggesting these locations were comparatively less impacted by point sources. Temporal fluctuations in N + N followed offshore seasonal trends (CT-DEEP 2021). The paucity of significant correlations between N + N and chl-*a* concentrations may have been due to AmN inhibiting N + N uptake, similar to other urban estuaries, although photo-acclimation in turbid nearshore areas may also explain the apparent lack of correlation (Parker et al., 2012; Glibert et al., 2022).

AmN concentrations were greater at sites near riverine and point source inputs (AC, CI, CP, SR) than RP, which lacks known input (Tetra Tech, 2018; New York State, 2022), indicating that terrestrial discharges influenced AmN shoreline delivery. While seasonal AmN trends (elevated concentrations fall versus winter, spring, and summer) at CI, RP, CP, and SR mirrored offshore (Humphries et al., 2023; Roldan-Ayala et al., 2023), the lack of synchrony with AC as well as the offset between AmN and N + N fluctuations, were further evidence of strong localized inputs and/or biogeochemical cycling processes regulating DIN availability. AmN concentrations at RP, CP, and SR were comparable in magnitude (0–7 μM) to offshore, with the more urbanized locations, CI (<1–10 μM) and AC (<1–22 μM), having relatively wider ranges (Humphries et al., 2023; Roldan-Ayala et al., 2023). Except for AC, AmN levels were within range of other urban estuaries, such as Chesapeake (<10 μM; Morse et al., 2014), Buzzards (3.3 μM; Turner et al., 2009), and San Francisco (SF) Bay estuaries (<5 μM; Glibert et al., 2022), the last value following WWT upgrades. Before upgrades, AmN reached ~90 μM near WWT plants in the SF Bay Delta, suppressing phytoplankton growth (most acutely diatoms) beginning at 10 μM (Glibert et al., 2016, 2022). In this study, AmN at all sites negatively correlated with chl-*a* across size fractions; similarly, N + N uptake rates were lowest in TG bioassay treatments with added AmN. Since AmN frequently exceeded 10 μM at AC, AmN-rich WW discharge likely inhibited phytoplankton (primarily diatoms) growth at both AC (adjacent to CSOs) and CP (downstream of the Norwalk River, which contains a WWT facility) (New York State, 2022; Tetra Tech, 2018). Although SR was adjacent to a WWT facility (Tetra Tech, 2018), AmN concentrations were <10 μM during surveys and thus unlikely to inhibit phytoplankton growth as N + N uptake was comparable among SR bioassay treatments. By comparison, RP, the site with no known freshwater or wastewater inputs, exhibited low mean DIN concentrations and the highest mean chl-*a* value among sites not directly adjacent to WW (CI, RP, and CP).

Concentrations of DIP fluctuated similarly across sites, with maximum concentrations during fall as offshore (Suter et al., 2014; Roldan-Ayala et al., 2023). Only AC had DIP concentrations above offshore maxima (6 μM; Roldan-Ayala et al., 2023), presumably from WW input. The lack of significant correlations between field DIP and chl-*a* combined with the paucity of linkages between phytoplankton and P additions during bioassays demonstrates that P did not limit phytoplankton in this study. AC and SR had the highest Si levels, suggesting they receive more mineral inputs. The East and Housatonic rivers have higher Si concentrations than the LIS mainstem (Gobler et al., 2006; Klug 2006) because those waters are enriched with clay and weathered rocks (Conley 1997), such that freshwater discharge of Si-rich water seasonally limits WLIS diatom growth and biomass (Gobler et al., 2006). Si concentrations at CI, RP, and CP fluctuated consistently, with maximum values during late summer and lowest during spring. Marked decreases in Si on March 08, 2021 following low precipitation coincided with diatom blooms at CI, RP, and CP, indicating drawdown. The similarity in seasonal fluctuations of Si and N + N concentrations at CI, RP, and CP, combined with their positive correlations preceding diatom blooms, showed that freshwater discharge of these nutrients co-limited diatom growth.

Shore chl-*a* concentration trends did not follow proximity to the heavily urbanized NYC, as SR values more closely resembled AC than other sites. This contrasts previous work showing chl-*a* concentrations (with a predominant contribution from cyanobacteria) generally increasing with urbanization across the LIS mainstem and indicates localized areas of high nearshore chl-*a* (Lopez et al., 2014; Perreira 2021; Roldan-Ayala et al., 2023), including synoptic observations across LIS from high spatial resolution satellite chl-*a* retrievals (Sherman et al., 2023a). These data underscore the importance of terrestrial influences on shore phytoplankton biomass and community composition. During cooler months, shore sites closely reflected the offshore biomass composition by cell size (Roldan-Ayala et al., 2023) as spring and fall contained greater chl-*a* contributions from the >20 μm cell size fraction (corresponding mostly but not exclusively to chain forming diatoms). This is consistent with both pre-(Capriulo et al., 2002; Suter et al., 2014; Li et al., 2018) and post-(Roldan-Ayala et al., 2023) COVID reports of diatoms being the dominant LIS taxon during these seasons, as they can contribute up to 61% of LIS mainstem phytoplankton species richness (Lopez et al., 2014).

At all sites, elevated total chl-*a* during summer (July and Aug.) coincided with low DIN, consistent with prior (pre-COVID) years (Rice and Stewart 2013; Lopez et al., 2014). Summer phytoplankton biomass was largely composed of nano- and picoplankton (<20 μm), with overall magnitude greater than offshore. Summer blooms at AC included mixotrophic flagellate taxa such as *Heterocapsa* spp. and euglenoids, presumably consuming commonly-occurring cyanobacteria such as *Synechococcus* spp. (Lopez et al., 2014). In the Chesapeake Bay, *Synechococcus* spp. thrives on regenerated nutrients during warmer seasons, as low DIN combined with high T favors growth of picoplankton over larger phytoplankton (Paerl et al., 2006; Morse et al., 2014; Anderson et al., 2022).

The summer assemblage contained a variety of dinoflagellates, including HAB forming species at all sites. HAB species that were observed but remained below bloom concentrations included the saxitoxin-producing genus *Alexandrium*, previously associated with WW effluent in Northport, NY (Hattenrath et al., 2010), *Margalefidinium polykrikoides*, associated with high DON in the LIS (Gobler et al., 2012), and *Dinophysis acuminata,* linked to high AmN in WLIS (Hattenrath--Lehmann et al., 2015).

By comparison, *P. triestinum* and *P. minimum* abundances were elevated during summer/fall, and *Heterocapsa* were observed year-round. *Prorocentrum* is a commonly-occurring LIS dinoflagellate genus (Lopez et al., 2014), and *P. triestinum* has been noted in urbanized areas of the Adriatic coast (Bužančić et al., 2016). The mixed *Prorocentrum* spp. bloom at RP on Aug. 05, 2021, which included bloom cell concentrations ($>1 \times 10^3$ cells mL^{-1}) of the okadaic acid-producing species *P. minimum*, were likely due to favorable DIN:DON conditions for dinoflagellate growth. *P. minimum* can bloom in response to anthropogenic DON (Glibert and Legrand 2006). *P. triestinium* responds to higher T and elevated nutrient concentrations with smaller cell sizes (phenotypic plasticity) and rapid growth rates, suggesting that climate change may promote this species in LIS (Flores-Moya et al., 2008). *Heterocapsa rotundata* proliferates in the Chesapeake Bay during colder months by consuming cyanobacteria in low light (Millette et al., 2016) and late-winter AC conditions (Mar. 08, 2021) provided similar environmental conditions. *Heterocapsa* was also frequently observed during summer at turbid sites AC and SR, including the mixed dinoflagellate species bloom (*Heterocapsa* and *Gymnodinium*) on Jul. 8, 2021 at AC, indicating this genus has a broad temperature niche and a selective advantage when light becomes limiting.

Euglenoids and mixotrophic cryptophytes were ubiquitous during summer, especially at the most turbid site, AC. These taxa prevail in eutrophic, low light estuarine systems, including the East River (Suter et al., 2014; Millette et al., 2016; Li et al., 2018). Euglenoids like *E. gracilis* can accelerate their growth rates with elevated T (Kitaya et al., 2005), indicating that euglenoids can thrive during warm months in turbid areas, where picoplankton may be available for consumption. The greater abundances of cryptophytes across shore sites compared to offshore (Lopez et al., 2014) aligns with their tendency to be common near N-rich, turbid freshwater (e.g., riverine) discharge (Suter et al., 2014; Griffiths et al., 2016). Overall, while the major phytoplankton taxa recorded in this study generally agree with pre-COVID LIS surveys (at Execution Rock, Milford CT, Oyster Bay LI, and CT shellfish monitoring sites), with numerous chain forming diatoms and euglenoids, cryptophytes, and dinoflagellates exhibiting seasonal blooms (Greenfield et al., 2005; Klug 2006; Van Gulick 2020), bioassay results suggest that their relative proportional abundances likely shifted during COVID-19 SIP.

During bioassays, the increase in total chl-*a* across treatments (including controls) suggested that neither N nor P limited WLIS productivity during the sampling period, in contrast with bioassays in freshwater systems that have shown P-limitation (Nwankwegu et al., 2020). Ubiquitous biomass growth also suggests a bottle effect, where separation from tidal flushing allowed optimal uptake of ambient and spiked nutrients (Gobler et al., 2006). The influence of N-form on phytoplankton assemblages was evident, particularly within the >20 μm cell size fraction. Increased abundances of chain-forming diatoms in spikes containing nitrate (*Thalassiosira* spp., *Skeletonema* spp., *Lithodesmium* sp. in NP at TG coupled with *Thalassiosira* spp., *Skeletonema* spp., *Leptocylindrus* sp., *Chaetoceros* sp. in ALL at SR) coincided with reductions in concentrations of N + N but not AmN. Diatoms downregulate AmN transporters with increasing AmN concentrations and upregulate N + N transporters with increasing N + N concentrations (Rogato et al., 2015; Glibert et al., 2016; Gao et al., 2018; Olofsson et al., 2019).

Previous bioassays found no phytoplankton assemblage linkages to N in the East River but responses to N + N were found across taxa in WLIS (Gobler et al., 2006), and diatom growth has been linked to N + N at the mouth of the Housatonic River (Klug 2006). Results herein suggest that during Sept. bioassays, diatom growth near the Narrows was primarily limited by N + N whereas at SR, farther east, diatoms were comparatively less N + N limited. Diatom growth rates at TG consistently demonstrated increased growth in NP. While the TG AP treatment exhibited elevated diatom growth compared to C, AmN was under-utilized, suggesting that phytoplankton growth may have been enhanced by a replicate(s) receiving more sunlight (less shading from nearby structures) despite randomization. At SR, elevated diatom growth rates did not appear to be linked with N-form. Interpolation of N + N linkages and concentration changes during bioassays with AmN inhibition during field surveys suggests there is an ideal DIN ratio (N + N:AmN) for diatom growth (Glibert 2019).

Since Sept. bioassays were after the July/Aug. dinoflagellate blooms, they presumably captured less N responses of these species. Flagellated species abundances decreased during each experiment, likely from being outcompeted by faster growing diatoms for nutrients and sunlight. In both experiments, the highest cryptophyte concentrations were in AP at t (72), with the highest growth rates also in AP, in agreement with rapid AmN uptake by the genus *Cryptomonas* compared to other N-forms (Cloern 1977; Egerton et al., 2014). At t (72), the presence of euglenoids in all TG treatments except NP, as well as increased abundances in all SR treatments except C and NP, shows this taxon does not compete well for N + N. Although bioassays only captured phytoplankton responses during Sept. 2021, they suggest that in the absence of elevated N + N, cryptophytes and euglenoids were successful competitors for AmN and presumably DON during shore sampling, particularly at sites with WW inputs. Alternatively, since smaller celled phytoplankton utilize AmN but have minimal capacity for N + N uptake in estuaries, increases in cryptophytes and euglenoid abundance may have been from increased heterotrophy of picoplankton, including cyanobacteria (Bradley et al., 2010; Glibert et al., 2016).

In contrast to DIN additions, the absence of distinct phytoplankton responses to urea demonstrates that DON levels did not limit

phytoplankton production, unlike other developed coastal systems such as Charleston, SC, where urea additions increased phytoplankton biomass (Reed et al., 2016). In WLIS, biologically available DON is elevated by WW effluent (Vaudrey et al., 2016). While WLIS DIN:DON has decreased from 2000 to 2021 (Whitney and Vlahos 2021), effluent contains substantial concentrations of AmN; therefore, N + N decreases suggest nitrate was the most limiting N-form for phytoplankton during this study.

Water sampling was not possible during spring 2020 due to pandemic restrictions, and while there is no long-term monitoring record of nearshore phytoplankton communities at these study sites for historical comparisons, bioassays mechanistically relate shore observations to N-form. Presumably low N + N throughout WLIS during COVID-19 SIP likely resulted in the general paucity of N + N, at shore sites with the exception of those that exhibited clear evidence of point source loading (AC and SR). Bioassays suggest these conditions contributed to a decline in diatom concentrations while providing favorable conditions for euglenoids and cryptophytes. These taxonomic shifts are similar to responses following WWT upgrades in the LIS region, where decreasing DIN:DON in WLIS resulted in declines in diatom abundances and increases in dinoflagellates, euglenoids, and cryptophytes (Suter et al., 2014). It has been additionally postulated that overall LIS cyanobacterial numbers have risen in tandem with decadal diatom declines (Gobler et al., 2006; Bradley et al., 2010; Suter et al., 2014). SIP orders likely produced similar shifts, as N + N concentrations measured here were often lower post-COVID compared to pre-COVID periods, and AmN inhibition was evident in both field and bioassay results. This may have explained the short-term 40% decrease in WLIS satellite-derived chl-*a* during Apr. 2020 (relative to 2017–2019) (Sherman et al., 2023b).

Results herein will be valuable for informing comparisons to long-term, pre-COVID water quality data and biogeochemical models that incorporate spatial and temporal trends in LIS N and phytoplankton. Given linkages between DIN-form and phytoplankton species composition, future work should continue to characterize the biogeochemical mechanism(s) of AmN inhibition throughout the WLIS related to phytoplankton assemblages. Future studies should also quantify compositional differences between nearshore and offshore phytoplankton communities, and though sample frequency differs, this work suggests nearshore concentrations of certain taxa (most strikingly euglenoids) are comparatively greater. Broader trophic connections should be explored as zooplankton exert top-down controls on phytoplankton N-uptake (Sailley et al., 2015), impacting nutrient cycling. Shifts in N form may also provide diazotrophs with a selective advantage (Berg et al., 2003; Knapp 2012), though this has not been explored within LIS. Finally, while this work suggests that while WW drives delivery of AmN and that rivers deliver a more balanced mixture of DIN forms, the influence of groundwater on N inputs should be explored. Biogeochemical models have shown the magnitude of subterraneous regenerated N + N delivered to the LIS may be comparable to the annual N delivered by WWT plants (Tamborski et al., 2020).

5. Management implications

While the response of the LIS phytoplankton community to WW upgrades over decades have been explored (Suter et al., 2014), and shorter term responses to upgrades have been identified in other systems (Gilbert et al., 2022), few papers have identified taxa specific linkages of nearshore phytoplankton communities to sudden shifts in available N form within urban waterways. This work suggests that diatoms are highly responsive to WLIS DIN form and concentration. Spring/summer phytoplankton biomass is hypothesized to influence hypoxia severity due to microbial respiration (decomposition) of organic matter following blooms (Anderson and Taylor 2001; Gobler et al., 2006; Perreira 2021). WW management should therefore consider the ecological consequences of limiting the diatom population via regulation of N + N and AmN concentrations in effluent, considering that higher N + N:AmN favors diatoms over dinoflagellates, including HAB species (Gobler et al., 2012). A "healthy" diatom assemblage may therefore help augment HAB management strategies (Nwankwegu et al., 2019).

6. Conclusion

Through shore surveys and bioassays, linkages between phytoplankton communities and DIN-form (Nov. 2020–Dec. 2021) were identified, capturing fall and winter COVID-19 waves. AmN was inversely related to biomass across cell size fractions and inhibited diatom growth, while N + N drove diatom growth throughout the WLIS. Euglenoids and cryptophytes demonstrated a preference for reduced (non-nitrate) N forms, especially AmN, and were frequently observed in WW-impacted shore samples. Likely decreases in N + N during COVID-19 SIP orders presumably reduced diatom concentrations; however, this phenomenon is complicated by the negative relationship of AmN to overall biomass. The duration and spatial extent of these assemblage shifts need further exploration as pandemic-related travel restrictions have eased and N-inputs to LIS have since risen. This work provides evidence for managing estuarine N-enrichment based on how localized differences in DIN-form and levels impact the phytoplankton community along an urban-suburban gradient.

Funding

Funding was courtesy of National Science Foundation awards #DEB-2039867 and #DEB-2039877, the Hudson River Foundation 2021 Tibor T. Polgar Fellowship, Environmental Protection Agency award #LI 96261317 Subaward #82913/2/1156439, the City University of New York Advanced Science Research Center, and National Aeronautics and Space Administration award NASA-RRNES/80NSSC20K1287.

Authors' declaration

I, on behalf of myself and co-authors, declare that this work has not been published previously and is not under consideration for publication elsewhere. If accepted, it will not be available elsewhere in the same form, in English or any other language, including electronically without written consent of the copyright-holder. I also declare that no AI was used in any way in the writing or preparation of this manuscript; presented work is original and our own.

CRediT authorship contribution statement

Maximillian Brown: Conceptualization, Formal analysis, Investigation, Methodology, Writing – original draft, Writing – review & editing. **Mariapaola Ambrosone:** Data curation, Formal analysis, Methodology, Resources, Writing – review & editing. **Kyle J. Turner:** Investigation, Methodology, Resources. **Georgie E. Humphries:** Investigation, Methodology. **Maria Tzortziou:** Conceptualization, Funding acquisition, Investigation, Project administration, Resources, Writing – review & editing. **Sílvia Anglès:** Conceptualization, Data curation, Formal analysis, Investigation, Methodology. **Caterina Panzeca:** Data curation, Funding acquisition, Investigation, Methodology, Resources, Writing – review & editing. **Dianne I. Greenfield:** Conceptualization, Data curation, Formal analysis, Funding acquisition, Investigation, Methodology, Project administration, Resources, Supervision, Validation, Writing – original draft, Writing – review & editing.

Declaration of competing interest

The authors declare that they have no known competing financial interests or personal relationships that could have appeared to influence the work reported in this paper.

Data availability

Data will be made available on request.

Acknowledgments

We thank SUNY Maritime and Sea Kayak Connecticut (Westport, CT) for dock access to conduct the bioassay experiments. We thank Dr. Stephen Gosnell and Dr. Gregory O'Mullan for manuscript feedback. We also thank Tzortziou lab members Dr. Brice Grunert and Alana Menendez for assistance collecting shore samples. Additional thanks to the Queens College Masters Scholarship for support.

Appendix A. Supplementary data

Supplementary data to this article can be found online at https://doi.org/10.1016/j.marenvres.2024.106371.

References

Anderson, T.H., Taylor, G.T., 2001. Nutrient pulses, plankton blooms, and seasonal hypoxia in western Long Island Sound. Estuaries 24, 228–243. https://doi.org/10.2307/1352947.

Anderson, S.I., Franzè, G., Kling, J.D., Wilburn, P., Kremer, C.T., Menden-Deuer, S., Litchman, E., Hutchins, D.A., Rynearson, T.A., 2022. The interactive effects of temperature and nutrients on a spring phytoplankton community. Limnol. Oceanogr. 67 (3), 634–645. https://doi.org/10.1002/lno.12023.

Berg, G.M., Balode, M., Purina, I., Bekere, S., Béchemin, C., Maestrini, S.Y., 2003. Plankton community composition in relation to availability and uptake of oxidized and reduced nitrogen. Aquat. Microb. Ecol. 30 (3), 263–274. https://doi.org/10.3354/ame030263.

Bock, E.M., Easton, Z.M., 2020. Export of nitrogen and phosphorus from golf courses: a review. J. Environ. Manag. 255, 109817 https://doi.org/10.1016/j.jenvman.2019.109817.

Bradley, P.B., Lomas, M.W., Bronk, D.A., 2010. Inorganic and organic nitrogen use by phytoplankton along Chesapeake Bay, measured using a flow cytometric sorting approach. Estuar. Coast 33 (4), 971–984. https://doi.org/10.1007/s12237-009-9252-y.

Braga, F., Ciani, D., Colella, S., Organelli, E., Pitarch, J., Brando, V.E., Bresciani, M., Concha, J.A., Giardino, C., Marco Scarpa, G., Volpe, G., Rio, M., Falcini, F., 2022. COVID-19 lockdown effects on a coastal marine environment: disentangling perception versus reality. Sci. Total Environ. 817, 153002 https://doi.org/10.1016/j.scitotenv.2022.153002.

Brown, R., 1984. Relationships between suspended solids, turbidity, light attenuation, and algal productivity. Lake Reservoir Manag. 1 (1), 198–205. https://doi.org/10.1080/07438148409354510.

Bužančić, M., Gladan, Ž.N., Marasović, I., Kuspilić, G., Grbec, B., 2016. Eutrophication influence on phytoplankton community composition in three bays on the eastern Adriatic coast. Oceanologia 58 (4), 302–316. https://doi.org/10.1016/j.oceano.2016.05.003.

Capriulo, G.M., Smith, G., Troy, R., Wikfors, G.H., Pellet, J., Yarish, C., 2002. The planktonic food web structure of a temperate zone estuary, and its alteration due to eutrophication. In: Orive, E., Elliott, M., de Jonge, V.N. (Eds.), Nutrients and Eutrophication in Estuaries and Coastal Waters. Springer, Dordrecht, pp. 263–333. https://doi.org/10.1007/978-94-017-2464-7_23.

Cira, E.K., Pearl, H.W., Wetz, M.S., 2016. Effects of nitrogen availability and form on phytoplankton growth in a eutrophied estuary (Neuse River Estuary, NC, USA). PLoS One, 0160663. https://doi.org/10.1371/journal.pone.0160663.

Cloern, J.E., 1977. Effects of light intensity and temperature on *Cryptomonas ovata* (Cryptophyceae) growth and nutrient uptake rates. J. Phycol. 13, 389–395. https://doi.org/10.1111/j.1529-8817.1977.tb02947.x.

Conley, D.J., 1997. Riverine contribution of biogenic silica to the oceanic silica budget. Limnol. Oceanogr. 42 (4), 774–777. https://doi.org/10.4319/lo.1997.42.4.0774.

Conway, H.L., Harrison, P.J., Davis, C.O., 1976. Marine diatoms grown in chemostats under silicate or ammonium limitation. II. Transient response of *Skeletonema costatum* to a single addition of the limiting nutrient. Mar. Biol. 35, 187–199. https://doi.org/10.1007/BF00390940.

CT-DEEP 2021, 2021. Long Island Sound hypoxia season review. https://portal.ct.gov/-/media/DEEP/water/lis_water_quality/monitoring/2021/2021-Combined-Report_final.pdf, 07 Oct. 2022).

Egerton, T.A., Morse, R.E., Marshall, H.G., Mulholland, M.R., 2014. Emergence of algal blooms: the effects of short-term variability in water quality on phytoplankton abundance, diversity, and community composition in a tidal estuary. Microorganisms 2 (1), 33–57. https://doi.org/10.3390/microorganisms2010033.

EPA National Estuary Program, 2022. Comprehensive Conservation and Management Plans. https://www.epa.gov/nep/comprehensive-conservation-and-management-plans#:~:text=The%20CCMP%20serves%20as%20a,fish%20and%20wildlife. (Accessed 17 November 2022).

EPA, 2012. Web Archive 2012, 5.7 Nitrates. https://archive.epa.gov/water/archive/web/html/vms57.html#:~:text=The%20natural%20level%20of%20ammonia,up%20to%2030%20mg%2FL. (Accessed 12 May 2023).

Fisher, S.C., Kephart, C.M., Cheung, N., Tagliaferri, T.N., 2022. Assessment of fecal contamination sources to Alley Creek, Queens County, New York, August 2020–June 2021. In: U.S. Geological Survey Scientific Investigations Report 2022–5068, p. 35. https://doi.org/10.3133/sir20225068.

Flores-Moya, A., Costas, E., López-Rodas, V., 2008. Roles of adaptation, chance and history in the evolution of the dinoflagellate *Prorocentrum triestinum*. Naturwissenschaften 95, 697–703. https://doi.org/10.1007/s00114-008-0372-1.

Gao, G., Xia, J., Yu, J., Zeng, X., 2018. Physiological response of a red tide alga (*Skeletonema costatum*) to nitrate enrichment, with special reference to inorganic carbon acquisition. Mar. Environ. Res. 133, 15–23. https://doi.org/10.1016/j.marenvres.2017.11.003.

Gay, P.S., O'Donnell, J., Edwards, C.A., 2004. Exchange between Long Island Sound and adjacent waters. J. Geophys. Res.: Oceans 109 (C6). https://doi.org/10.1029/2004JC002319.

Glibert, P.M., Legrand, C., 2006. The diverse nutrient strategies of harmful algae: focus on osmotrophy. In: Granéli, E., Turner, J. (Eds.), Ecology of Harmful Algae. Springer, Berlin, pp. 163–175.

Glibert, P.M., Wilkerson, F.P., Dugdale, R.C., Raven, J.A., Dupont, C.L., Leavitt, P.R., Parker, A.E., Burkholder, J.M., Kana, T.M., 2016. Pluses and minuses of ammonium and nitrate uptake and assimilation by phytoplankton and implications for productivity and community composition, with emphasis on nitrogen-enriched conditions. Limnol. Oceanogr. 61 (1), 165–197. https://doi.org/10.1002/lno.10203.

Glibert, P.M., 2019. Phytoplankton in the aqueous ecological theater: changing conditions, biodiversity, and evolving ecological concepts. J. Mar. Res. 77, 83–137. Supplement. https://elischolar.library.yale.edu/journal_of_marine_research/474.

Glibert, P.M., Wilkerson, F.P., Dugdale, R.C., Parker, A.E., 2022. Ecosystem recovery in progress? Initial nutrient and phytoplankton response to nitrogen reduction from sewage treatment upgrade in the San Francisco Bay Delta. Nitrogen 3 (4), 569–591. https://doi.org/10.3390/nitrogen3040037.

Gobler, C.J., Buck, N.J., Sieracki, M.E., Sañudo-Wilhelmy, S.A., 2006. Nitrogen and silicon limitation of phytoplankton communities across an urban estuary: the East River-Long Island Sound system. Estuar. Coast Shelf Sci. 68 (1–2), 127–138. https://doi.org/10.1016/j.ecss.2006.02.001.

Gobler, C.J., Burson, A., Koch, F., Tang, Y., Mulholland, M.R., 2012. The role of nitrogenous nutrients in the occurrence of harmful algal blooms caused by *Cochlodinium polykrikoides* in New York estuaries (USA). Harmful Algae 17, 64–74. https://doi.org/10.1016/j.hal.2012.03.001.

Grasshoff, K., Kremling, K., Ehrhardt, M., 1999. Methods of Seawater Analysis, third ed. Wiley, Weinheim.

Greenfield, D.I., Lonsdale, D.J., Cerrato, R.M., 2005. Linking phytoplankton community composition with juvenile-phase growth in the Northern Quahog *Mercenaria mercenaria*. Estuaries 28, 241–251. https://doi.org/10.1007/BF02732858.

Griffiths, J.R., Hajdu, S., Downing, A.S., Hjerne, O., Larsson, U., Winder, M., 2016. Phytoplankton community interactions and environmental sensitivity in coastal and offshore habitats. Oikos 125 (8), 1134–1143. https://doi.org/10.1111/oik.02405.

Hales, B., van Geen, A., Takahashi, T., 2004. High-frequency measurement of seawater chemistry: flow-injection analysis of macronutrients. Limnol Oceanogr. Methods 2, 91–101. https://doi.org/10.4319/lom.2004.2.91.

Hattenrath, T.K., Anderson, D.M., Gobler, C.J., 2010. The influence of anthropogenic nitrogen loading and meteorological conditions on the dynamics and toxicity of *Alexandrium fundyense* blooms in a New York (USA) estuary. Harmful Algae 9, 402–412. https://doi.org/10.1016/j.hal.2010.02.003.

Hattenrath-Lehmann, T.K., Marcoval, M.A., Mittlesdorf, H., Goleski, J.A., Wang, Z., Haynes, B., Morton, S.L., Gobler, C.J., 2015. Nitrogenous nutrients promote the growth and toxicity of *Dinophysis acuminata* during estuarine bloom events. PLoS One 10 (4), e0124148. https://doi.org/10.1371/journal.pone.0124148.

Humphries, G.E., Espinosa, J.I., Ambrosone, M., Roldan-Ayala, Z., Tzortziou, M., Goes, J. I., Greenfield, D.I., 2023. Transitions in nitrogen and organic matter form and concentration correspond to bacterial population dynamics in a hypoxic urban estuary. Biogeochemistry 163 (2), 219–243. https://doi.org/10.1007/s10533-023-01021-2.

Kitaya, Y., Azuma, H., Kiyota, M., 2005. Effects of temperature, CO2/O2 concentrations and light intensity on cellular multiplication of microalgae, *Euglena gracilis*. Adv. Space Res. 35 (9), 1584–1588. https://doi.org/10.1016/j.asr.2005.03.039.

Klug, J.L., 2006. Nutrient limitation in the lower Housatonic River estuary. Estuar. Coast 29 (5), 831–840. https://doi.org/10.1007/BF02786534.

Knapp, A.N., 2012. The sensitivity of marine N2 fixation to dissolved inorganic nitrogen. Front. Microbiol. 3, 374. https://doi.org/10.3389/fmicb.2012.00374.

LeGresley, M., McDermott, G., 2010. Counting chamber methods for quantitative phytoplankton analysis - haemocytometer, Palmer-Maloney cell and Sedgewick-Rafter cell. In: Intergovernmental Oceanographic Commission Manuals and Guides 55: Microscopic and Molecular Methods for Quantitative Phytoplankton Analysis. UNESCO, pp. 25–30.

Lemley, D.A., Adams, J.B., Bornman, T.G., Campbell, E.E., Deyzel, S.H., 2019. Land-derived inorganic nutrient loading to coastal waters and potential implications for nearshore plankton dynamics. Continent. Shelf Res. 174, 1–11. https://doi.org/10.1016/j.csr.2019.01.003.

Li, Y.S.L., Meseck, M.S., Dixon, 2018. The East River tidal strait, New York City, New York, a high-nutrient, low-chlorophyll coastal system. Int. Aquat. Res. 10, 65–77. https://doi.org/10.1007/s40071-018-0189-2.

Liu, D., Yang, H., Thompson, J.R., Li, J., Loiselle, S., Duan, H., 2022. COVID-19 lockdown improved river water quality in China. Sci. Total Environ. 802, 149585 https://doi.org/10.1016/j.scitotenv.2021.149585.

Long Island Sound Study, 2021. Long Island Sound- by the Numbers. https://longislandsoundstudy.net/. (Accessed 8 August 2021).
Lonsdale, D.J., Greenfield, D.I., Hillebrand, E.M., Nuzzi, R., Taylor, G.T., 2006. Contrasting microplanktonic composition and food web structure in two coastal embayments (Long Island, NY, USA). J. Plankton Res. 28, 891–905. https://doi.org/10.1093/plankt/fbl027.
Lopez, G., Carey, D., Carlton, J.T., Cerrato, R., Dam, H., Digiovanni, R., Elphick, C., Michael, F., Gobler, C., Hice, L., Howell, P.A., Jordaan, A., Lin, S., Liu, S., Lonsdale, D., Mcenroe, M., Mckown, K., Mcmanus, G., Orson, R., Peterson, B., Pickerell, C., Rozsa, R., Shumway, S.E., Siuda, A., Streich, K., Talmage, S., Taylor, G., Thomas, E., Van Patten, M., Vaudrey, J., Yarish, C., Wikfors, G.H., Zajac, R., 2014. Chapter 6: Biology and Ecology of Long Island Sound. In: Latimer, J.S., Tedesco, M. A., Swanson, R.L., Yarish, C., Stacey, P.E., Garza, C. (Eds.), Long Island Sound: Prospects for the Urban Sea. Springer, New York, pp. 285–479.
Mallick, S.P., Mallick, Z., Mayer, B.K., 2022. Meta-analysis of the prevalence of dissolved organic nitrogen (DON) in water and wastewater and review of DON removal and recovery strategies. Sci. Total Environ. 154476 https://doi.org/10.1016/j.scitotenv.2022.154476.
Mallin, M.A., McIver, M.R., Wambach, E.J., Robuck, A.R., 2016. Algal blooms, circulators, waterfowl, and eutrophic Greenfield Lake, North Carolina. Lake Reservoir Manag. 32 (2), 168–181. https://doi.org/10.1080/10402381.2016.1146374.
McCarthy, M.J., James, R.T., Chen, Y., East, T.L., Gardner, W.S., 2009. Nutrient ratios and phytoplankton community structure in the large, shallow, eutrophic, subtropical Lakes Okeechobee (Florida, USA) and Taihu (China). Limnology 10, 215–227. https://doi.org/10.1007/s10201-009-0277-5.
Millette, N.C., Pierson, J.J., Aceves, A., Stoecker, D.K., 2016. Mixotrophy in *Heterocapsa rotundata*: a mechanism for dominating the winter phytoplankton. Limnol. Oceanogr. 62 (2), 836–845. https://doi.org/10.1002/lno.10470.
Mishra, D.R., Kumar, A., Muduli, P.R., Equeenuddin, S.M., Rastogi, G., Acharyya, T., Swain, D., 2020. Decline in phytoplankton biomass along Indian coastal waters due to COVID-19 lockdown. Rem. Sens. 12 (16), 2584. https://doi.org/10.3390/rs12162584.
Miskewitz, R., Uchrin, C., 2013. In-stream dissolved oxygen impacts and sediment oxygen demand resulting from combined sewer overflow discharges. J. Environ. Eng. 139 (10), 1307–1313. https://doi.org/10.1061/(ASCE)EE.1943-7870.0000739.
Morse, R.E., Mulholland, M.R., Egerton, T.A., Marshall, H.G., 2014. Phytoplankton and nutrient dynamics in a tidally dominated eutrophic estuary: daily variability and controls on bloom formation. Mar. Ecol. Prog. Ser. 503, 59–74. https://doi.org/10.3354/meps10743.
National Oceanic and Atmospheric Administration, 2023. Nautical Chart 12364: New Haven Harbor Entrance and Port Jefferson to Throgs Neck [Mercator Projection]. 1: 40,000. Washington, D.C. Updated 09 Aug.
National Weather Service, 2022. NOAA Online Weather Data. https://www.weather.gov/wrh/Climate?wfo=okx. (Accessed 18 November 2022).
New York Department of Environmental Protection, 2022a. Harbor Water Quality. https://data.cityofnewyork.us/Environment/Harbor-Water-Quality/5uug-f49n. (Accessed 4 January 2022).
New York Department of Environmental Protection, 2022b. Waste Water Treatment Process. In: https://www.nyc.gov/site/dep/water/wastewater-treatment-process.page. (Accessed 21 December 2022).
New York State, 2022. Combined Sewer Overflows (CSOs) Map. Data. Gov, Ny. https://data.ny.gov/Energy-Environment/Combined-Sewer-Overflows-CSOs-Map/i8hd-rmbi. (Accessed 7 October 2022).
New York State Governor, 2021. Executive Order 210: Expiration of Orders 202 and 205. https://www.governor.ny.gov/sites/default/files/2021-06/EO_210.pdf. (Accessed 21 December 2022).
New York State Department of Environmental Conservation, 2017. Department Approval for Alley Creek Long Term Control Plan. https://www.nyc.gov/assets/dep/downloads/pdf/water/nyc-waterways/alley-creek/2017-03-07-dec-app-alley-creek-ltcp.pdf. (Accessed 21 December 2022).
Nwankwegu, A.S., Li, Y., Huang, Y., Wei, J., Norgbey, E., Sarpong, L., Lai, Q., Wang, K., 2019. Harmful algal blooms under changing climate and constantly increasing anthropogenic actions: the review of management implications. 3 Biotech 9, 1–19. https://doi.org/10.1007/s13205-019-1976-1.
Nwankwegu, A.S., Li, Y., Huang, Y., Wei, J., Norgbey, E., Lai, Q., Sarpong, L., Wang, K., Ji, D., Yang, Z., Paerl, H.W., 2020. Nutrient addition bioassay and phytoplankton community structure monitored during autumn in Xiangxi Bay of Three Gorges Reservoir, China. Chemosphere 247, 125960. https://doi.org/10.1016/j.chemosphere.2020.125960.
O'Donnell, J., Wilson, R.E., Lwiza, K., Whitney, M., Bohlen, W.F., Codiga, D., Fribance, D.B., Fake, T., Bowman, M., Varekamp, J., 2014. The physical oceanography of Long Island Sound. In: Latimer, J.S., Tedesco, M.A., Swanson, R.L., Yarish, C., Stacey, P.E., Garza, C. (Eds.), Long Island Sound: Prospects for the Urban Sea. Springer, New York, pp. 79–158.
Olofsson, M., Robertson, E.K., Edler, L., Arneborg, L., Whitehouse, M.J., Ploug, H., 2019. Nitrate and ammonium fluxes to diatoms and dinoflagellates at a single cell level in mixed field communities in the sea. Sci. Rep. 9, 1–12. https://doi.org/10.1038/s41598-018-38059-4.
Paerl, H.W., Valdes, L.M., Peierls, B.L., Adolf, J.E., Harding, L.J.W., 2006. Anthropogenic and climatic influences on the eutrophication of large estuarine ecosystems. Limnol. Oceanogr. 51, 448–462. https://doi.org/10.4319/lo.2006.51.1_part_2.0448.
Parker, A.E., Dugdale, R.C., Wilkerson, F.P., 2012. Elevated ammonium concentrations from wastewater discharge depress primary productivity in the Sacramento River and the Northern San Francisco Estuary. Mar. Pollut. Bull. 64 (3), 574–586. https://doi.org/10.1016/j.marpolbul.2011.12.016.
Perreira, S., 2021. Long Term Nutrient and Chlorophyll a Dynamics across Long Island Sound and Impacts on Dissolved Oxygen Conditions within the Western Sound (1991-2019). Master's Thesis, City College of New York,. City University of New York, p. 45. https://academicworks.cuny.edu/cc_etds_theses/961/.
Pinckney, J.L., Knotts, E.R., Kibler, K.J., Smith, E.M., 2020. Nutrient breakpoints for estuarine phytoplankton communities. Limnol. Oceanogr. 65 (12), 2999–3016. https://doi.org/10.1002/lno.11570.
Polikarpov, I., Al-Yamani, F., Petrov, P., Saburova, M., Mihalkov, V., Al-Enezi, A., 2021. Phytoplankton bloom detection during the COVID-19 lockdown with remote sensing data: using Copernicus Sentinel-3 for north-western Arabian/Persian Gulf case study. Mar. Pollut. Bull. 171 https://doi.org/10.1016/j.marpolbul.2021.112734, 112734.
Redfield, A.C., 1958. The biological control of chemical factors in the environment. Am. Sci. 46, 205–221.
Reed, M., DiTullio, J., Kacenas, S., Greenfield, D.I., 2015. Effects of nitrogen and dissolved organic carbon on microplankton abundances in four coastal South Carolina systems. Aquat. Microb. Ecol. 76, 1–14. https://doi.org/10.3354/ame01764.
Reed, M.L., Pinckney, J.L., Keppler, C.J., Brock, L.M., Hogan, S.B., Greenfield, D.I., 2016. The influence of nitrogen and phosphorus on phytoplankton growth and assemblage composition in four coastal, southeastern USA systems. Estuar. Coast Shelf Sci. 177, 71–82. https://doi.org/10.1016/j.ecss.2016.05.002.
Rice, E., Stewart, G., 2013. Analysis of interdecadal trends in chlorophyll and temperature in the central basin of Long Island Sound. Estuar. Coast Shelf Sci. 128, 64–75. https://doi.org/10.1016/j.ecss.2013.05.002.
Roldan-Ayala, Z., Arnott, S.A., Ambrosone, M., Espinosa, J., Humphries, G., Tzortziou, M., Goes, J., Greenfield, D.I., 2023. The influences of phenology, spatial distribution, and nitrogen form on Long Island Sound phytoplankton biomass and taxonomic composition. Estuar. Coast Shelf Sci. 292, 108451 https://doi.org/10.1016/j.ecss.2023.108451.
Rogato, A., Amato, A., Iudicone, D., Chiurazzi, M., Ferrante, M.I., d'Alcalà, M.R., 2015. The diatom molecular toolkit to handle nitrogen uptake. Mar. Genomics 24, 95–108. https://doi.org/10.1016/j.margen.2015.05.018.
Romero, E., Peters, F., Arin, L., Guillén, J., 2014. Decreased seasonality and high variability of coastal plankton dynamics in an urban location of the NW Mediterranean. J. Sea Res. 88, 130–143. https://doi.org/10.1016/j.seares.2014.01.010.
Rutz, C., Loretto, M.C., Bates, A.E., Davidson, S.C., Duarte, C.M., Jetz, W., Johnson, M., Kato, A., Kays, R., Mueller, T., Primack, R.B., 2020. COVID-19 lockdown allows researchers to quantify the effects of human activity on wildlife. Nat. Ecol. Evol. 4 (9), 1156–1159. https://doi.org/10.1038/s41559-020-1237-z.
Sailley, S.F., Polimene, L., Mitra, A., Atkinson, A., Allen, J.I., 2015. Impact of zooplankton food selectivity on plankton dynamics and nutrient cycling. J. Plankton Res. 37 (3), 519–529. https://doi.org/10.1093/plankt/fbv020.
Sala, M.M., Peters, F., Sebastián, M., Cardelús, C., Calvo, E., Marrasé, C., Massana, R., Pelejero, C., Sala-Coromina, J., Vaqué, D., Gasol, J.M., 2022. COVID-19 lockdown moderately increased oligotrophy at a marine coastal site. Sci. Total Environ. 812, 151443 https://doi.org/10.1016/j.scitotenv.2021.151443.
Schweitzer, K., 2019. The Seasonal and Spatial Effects of a Sewage Outfall on the Planktonic Community Composition and Abundance. Doctoral Dissertation, State University of New York at Stony Brook, p. 24. https://www.proquest.com/openview/6549c6b2c588d8910c7741ba65a0795d/1?pq-origsite=gscholar&cbl=2026366&diss=y.
Sherman, J., Tzortziou, M., Turner, K.J., Goes, J., Grunert, B., 2023. Chlorophyll dynamics from Sentinel-3 using an optimized algorithm for enhanced ecological monitoring in complex urban estuarine waters. Int. J. Appl. Earth Obs. Geoinf. 118, 103223 https://doi.org/10.1016/j.jag.2023.103223 (a).
Sherman, J., Tzortziou, M., Turner, K.J., Greenfield, D.I., Menendez, A., 2023b. Deciphering the Water Quality Impacts of COVID-19 Human Mobility Shifts in Estuaries surrounding New York City. Science of the Total Environment, 896164953. https://doi.org/10.1016/j.scitotenv.2023.164953.
Sitta, K., Callahan, T., Doll, C., Mortensen, R., Reed, M., Greenfield, D.I., 2018. The influences of nitrogen form and zooplankton grazing on phytoplankton assemblages in two coastal southeastern systems. Limnol. Oceanogr. 63 (6), 2523–2544.
Suter, E.A., Lwiza, K.M., Rose, J.M., Gobler, C., Taylor, G.T., 2014. Phytoplankton assemblage changes during decadal decreases in nitrogen loadings to the urbanized Long Island Sound estuary, USA. Mar. Ecol. Prog. Ser. 497, 51–67. https://doi.org/10.3354/meps10602.
Tamborski, J., Cochran, J.K., Bokuniewicz, H., Heilbrun, C., Garcia-Orellana, J., Rodellas, V., Wilson, R., 2020. Radium mass balance sensitivity analysis for submarine groundwater discharge estimation in semi-enclosed basins: the case study of Long Island Sound. Front. Environ. Sci. 8 (108) https://doi.org/10.3389/fenvs.2020.00108.
Tetra Tech, 2018. Establishing nitrogen endpoints for three Long Island Sound watershed groupings: embayments, large riverine systems, and Western Long Island Sound open water. Commissioned by the EPA. https://longislandsoundstudy.net/wp-content/uploads/2018/06/A-Embayment-and-Western-LIS-N-Loading.pdf.
Trygar, R., 2009. Nitrogen Control in Wastewater Treatment Plants, second ed. University of Florida Center for Training, Research and Education for Environmental Occupations (TREEO) https://treeo.ufl.edu/media/treeoufledu/waterwastewater/student-resources/Nitrogen-control-in–wastewater-treatment-plants-v4.pdf. (Accessed 17 November 2022).
Turner, J.T., Lincoln, J.A., Borkman, D.G., Gauthier, D.A., Kieser, J.T., Dunn, C.A., 2000. Nutrients, Eutrophication and Harmful Algal Blooms in Buzzards Bay,

Massachusetts. Final Report submitted to Massachusetts Department of Environmental Protection, Project, p. 140.
Turner, J.T., Borkman, D.G., Lincoln, J.A., Gauthier, D.A., Petitpas, C.M., 2009. Plankton studies in Buzzards Bay, Massachusetts, USA. VI. Phytoplankton and water quality, 1987 to 1998. Mar. Ecol. Prog. Ser. 376, 103–122. https://doi.org/10.3354/meps07783.
Tzortziou, M., Kwong, C.F., Goldberg, D., Schiferl, L., Commane, R., Abuhassan, N., Szykman, J.J., Valin, L.C., 2022. Declines and peaks in NO2 pollution during the multiple waves of the COVID-19 pandemic in the New York metropolitan area. Atmos. Chem. Phys. 22, 2399–2417. https://doi.org/10.5194/acp-22-2399-2022.
United States Census Bureau, 2020. Census Demographic Map Viewer. https://mtgis-portal.geo.census.gov/arcgis/apps/MapSeries/index.html?appid=2566121a73de463995ed2b2fd7ff6eb7. (Accessed 17 November 2022).
United States Census Bureau, 2022. Population Estimates. US Census Quick Facts. https://www.census.gov/quickfacts/fact/table/westporttownfairfieldcountyconnecticut,newyorkcitynewyork/PST045221. (Accessed 15 December 2022).
United States Geological Survey, 2022. Monitoring Location 01209500. https://waterdata.usgs.gov/monitoring-location/01209500/#parameterCode=00065&period=P7D. (Accessed 15 December 2022).
Van Gulick, E., 2020. 2020 Conneticut Harmful Algal Bloom Report. CT Department of Agriculture. https://portal.ct.gov/-/media/DOAG/Aquaculture/HABs/2020-Connecticut-HAB-Report.pdf. (Accessed 15 December 2022).
Vaudrey, J.M.P., Yarish, C., Kim, J.K., Pickerell, C., Brousseau, L., Eddings, J., Sautkulis, M., 2016. Connecticut Sea Grant project report: comparative analysis and model development for determining the susceptibility to eutrophication of Long Island Sound embayments. Project number R/CE-34-CTNY. 46. https://longislandsoundstudy.net/wp-content/uploads/2013/08/Vaudrey_R-CE-34-CTNY_FinalReport_2016.pdf. (Accessed 15 December 2022).
Vaudrey, J., 2017. New York City's Impact on Long Island Sound Water Quality Technical Report. Report to Save the Sound, New Haven, CT.
Vlahos, P., Whitney, M.M., Menniti, C., Mullaney, J.R., Morrison, J., Jia, Y., 2020. Nitrogen budgets of the long Island Sound estuary. Estuar. Coast Shelf Sci. 232, 106493 https://doi.org/10.1016/j.ecss.2019.106493.
Welschmeyer, N.A., 1994. Fluorometric analysis of chlorophyll a in the presence of chlorophyll b and phaeopigments. Limnol. Oceanogr. 39, 1985–1992. https://doi.org/10.4319/LO.1994.39.8.1985.
Whitney, M.M., Vlahos, P., 2021. Reducing hypoxia in an urban estuary despite climate warming. Environ. Sci. Technol. 55, 941–951. https://doi.org/10.1021/acs.est.0c03964.
Yao, X., Sipler, R.E., Stanley, B.C., Roberts, Q.N., Sanderson, M.P., Bott, C.B., Bronk, D. A., 2019. Quantifying effluent dissolved organic nitrogen (EDON) uptake by microbial communities along a salinity gradient in the York River. Estuar. Coast 42, 1265–1280. https://doi.org/10.1007/s12237-019-00563-9.
Yoon, J.E., Son, S., Kim, I.N., 2022. Capture of decline in spring phytoplankton biomass derived from COVID-19 lockdown effect in the Yellow Sea offshore waters. Mar. Pollut. Bull. 174, 113175 https://doi.org/10.1016/j.marpolbul.2021.113175.
Zimmerman, C.F., Keefe, C.W., 1991. Determination of Nitrate + Nitrite in Estuarine and Coastal Waters by Automated Colorimetric Analysis. An Interim Manual of Methods for the Determination of Nutrients in Estuarine and Coastal Waters. Revision, 1. EPA Method 353.4. Cincinnati, OH.